bioRxiv preprint doi: https://doi.org/10.1101/2024.06.27.600930; this version posted July 2, 2024. The copyright holder for this preprint (which was not certified by peer review) is the author/funder, who has granted bioRxiv a license to display the preprint in perpetuity. It is made available under aCC-BY-NC-ND 4.0 International license.

Cellular and Molecular Changes During Aging in MEC: Unveiling the Role of Bglap3 Neurons in Cognitive Aging

Qichen Cao[1,3,7], Sorgog Uzeen[1,2,3,7], Sihui Cheng[1,3,4,7], Yuanjing Liu[1,3,7], Jiangyuan Liu[1,3,4], Shidan Wen[1,3], Meng Zhong[1,3], Jun Hao[1,3], Shuyang Yao[1,3], Yikai Yang[1,3], Xingyu Yan[1,3], Weixiang Guo[5,6], Chenglin Miao[1,2,3,4,7*]

1. State Key Laboratory of Membrane Biology, School of Life Sciences, Peking University, Beijing, 100871, China.
2. Peking University-Tsinghua University-National Institute of Biological Sciences Joint Graduate Program, Academy for Advanced Interdisciplinary Studies, Peking University, Beijing 100871, China.
3. PKU-IDG/McGovern Institute for Brain Research, Peking University, Beijing, 100871, China.
4. Peking-Tsinghua Center for Life Sciences, Beijing, 100871, China.
5. State Key Laboratory for Molecular and Developmental Biology, Institute of Genetics and Developmental Biology, Chinese Academy of Sciences, Beijing 100101, China.
6. Graduate School, University of Chinese Academy of Sciences, Beijing 100093, China.
7. These authors contributed equally to this study.

*Corresponding author:

Chenglin Miao, chenglin.miao@pku.edu.cn

bioRxiv preprint doi: https://doi.org/10.1101/2024.06.27.600930; this version posted July 2, 2024. The copyright holder for this preprint (which was not certified by peer review) is the author/funder, who has granted bioRxiv a license to display the preprint in perpetuity. It is made available under aCC-BY-NC-ND 4.0 International license.

Summary

Aging-correlated cognitive declines, including deficiencies in spatial orientation and memory, may reflect dysfunction in the hippocampus and medial entorhinal cortex (MEC). However, aging-related changes in MEC at the cellular and molecular levels remain unclear. In this study, we found fewer grid cells with reduced spatial stability in old mice. We compared gene expression profiles between young and old mice using 10x Genomics Visium technology. Among 1664 differentially expressed genes, we discovered Bglap3, a marker gene for subpopulation in MEC Layer III with decreased cell number with age. Silencing of Bglap3+ neurons in young mice impaired the spatial tuning of neurons in MEC and the spatial learning of a new platform location in water maze. These findings help us to understand the cellular and molecular changes in the MEC in healthy aging animals and the changes of Bglap3+ cells in old mice indicating a possible cause of aging-related MEC deficiency.

Keywords Navigation, grid cell, aging, spatial transcriptomics

Introduction

Cognitive decline, which includes pathological features such as spatial memory deficiency, is one of the biggest challenges faced by older people in aging societies [1,2]. Based on their discovery in most species, including humans [3,4], nonhuman primates [5], dogs [6], rats [7], and

bioRxiv preprint doi: https://doi.org/10.1101/2024.06.27.600930; this version posted July 2, 2024. The copyright holder for this preprint (which was not certified by peer review) is the author/funder, who has granted bioRxiv a license to display the preprint in perpetuity. It is made available under aCC-BY-NC-ND 4.0 International license.

mice [8], age-related cognitive deficiencies in spatial learning and memory are evolutionarily conserved. Therefore, it is important to conduct animal studies to understand the underlying mechanism of age-related cognitive decline in humans. The medial entorhinal cortex (MEC) is a key component of the mammalian neural circuit for the representation of space [9,10], and it is the area of the memory circuit that is affected early in aging-related cognitive decline [11,12]. MEC lesions impair spatial learning and memory [13], and disrupted grid coding impairs path integration in mice [14]. Understanding changes in the MEC during aging at the cellular and molecular levels could help to gain insight into the mechanism of aging-related decline in spatial learning and memory.

The grid cell was the first functional cell type to be described in the MEC [15]. In an open environment, grid cells fire action potentials at locations that form a hexagonal grid that spans the entire space. Grid cells are embedded with functionally distinct MEC cell types, including head direction cells [16], border cells [17,18], and speed cells [19,20]. This wider network interacts with specialized cells in neighboring brain regions, such as object cells in the lateral entorhinal cortex [21,22], and place cells [23] and goal-vector cells [24,25] in the hippocampus. Collectively, the assemblage of functional entorhinal and hippocampal cell types provides animals with a dynamic representation of space that enables navigation. In the hippocampus, hippocampal place cells are the major neuron type [23] that selectively code the spatial locations of animals. Previous research revealed that place cells become unstable between experimental sessions in older rats [7]. Similar deficiencies in the hippocampus and parahippocampal regions have

bioRxiv preprint doi: https://doi.org/10.1101/2024.06.27.600930; this version posted July 2, 2024. The copyright holder for this preprint (which was not certified by peer review) is the author/funder, who has granted bioRxiv a license to display the preprint in perpetuity. It is made available under aCC-BY-NC-ND 4.0 International license.

also been found in old humans when navigating in a virtual environment [3]. These findings suggest that changes in the hippocampus may contribute to the decline in spatial learning and memory during aging. Changes in grid coding of the MEC, one synapse upstream of the hippocampus, have been reported during normal aging in humans using fMRI [26]. Grid cells in the MEC as well as spatial memory were shown to be impaired in transgenic mice expressing mutant human tau [27], indicating that changes in grid cells might be related to the development of Alzheimer's disease (AD). In addition, grid cell-like activity was found to be impaired in young human adults carrying the APOE-ε4 allele and at risk of developing AD [28]. However, the changes in the number of grid cells during normal aging remain undetermined. Moreover, it is unclear whether other populations of neurons—such as head direction cells, border cells, and speed cells—are affected in the MEC during normal aging. Previous research revealed that aging did not affect neural populations in the brain equally [29], with some neural populations becoming deficient and others remaining unaffected. However, it is unknown whether different types of spatial cells in the MEC exhibit distinct changes during aging.

Aging is often related to transcriptomic changes accumulated over time and it is often not a universal change due to the complex heterogeneity of cell population in the brain [30]. Given the fact that MEC contains many different neuronal subtypes identified by their unique molecular markers that form unique projecting patterns inside MEC and to the hippocampus [15,31], it is important to rule out what happened to these neuronal subtypes or subregions

bioRxiv preprint doi: https://doi.org/10.1101/2024.06.27.600930; this version posted July 2, 2024. The copyright holder for this preprint (which was not certified by peer review) is the author/funder, who has granted bioRxiv a license to display the preprint in perpetuity. It is made available under aCC-BY-NC-ND 4.0 International license.

during aging that might lead to a decline on certain cognitive level. Previous studies have done comprehensive work on aging mouse brains to reveal transcriptomic changes happening in various brain regions through the use of bulk sequencing and single-cell sequencing[32–34]. Nevertheless, these methods cannot fully explain the *in situ* changes. Furthermore, currently developed spatial sequencing technologies have not explored the MEC during aging [35–38]. Therefore, it is important to investigate the transcriptomic changes of MEC *in situ* during aging.

In the present study, we directly compared the function of different neural populations in the MEC between young (3–4 months) and old (> 28 months) mice based on extracellular recordings in freely behaving mice. We also utilized the 10x Genomics Visium technology, which reduces tissue dissociation-related cell death and efficiently recovers RNA from old brain tissue, to examine the high-throughput expression profile in the MEC during aging. Furthermore, by conducting chemogenetic silencing and two-photon microscope (TPM) calcium imaging, we identified Bglap3+ neural populations that have a potential relationship with age-related cognitive decline, and that inactivation of Bglap3+ cells impaired the spatial learning of young mice. These findings allow us to understand the changes in spatial coding, molecular profile, and the related circuitry mechanisms during normal aging in MEC.

bioRxiv preprint doi: https://doi.org/10.1101/2024.06.27.600930; this version posted July 2, 2024. The copyright holder for this preprint (which was not certified by peer review) is the author/funder, who has granted bioRxiv a license to display the preprint in perpetuity. It is made available under aCC-BY-NC-ND 4.0 International license.

Results

Experimental strategy to record spatial cells in the MEC of young and old mice

To determine whether normally aged mice exhibited any changes in spatial coding of the MEC, we performed tetrode recording in the MEC of 5 young (3–4 months) and 10 old (>28 months) C57BL/6J mice. All tetrode traces were located in the dorsomedial MEC (Figure 1A and S1). There was no significant difference in running speed between the young and old mice (young mice: 26.1 ± 1.10 cm/s; old mice: 25.4 ± 1.11 cm/s; two-sample t-test, $t(190) = 0.42$, $P = 0.67$). The coverage of the box was also unaltered (young mice: 88.9 ± 0.28%; old mice: 88.4 ± 0.25%; two-sample t-test, $t(190) = 1.37$, $P = 0.17$).

Spatial tuning of grid cells was impaired in old mice

A total of 930 cells were collected with tetrode recording, of which 393 cells were collected from young mice and 537 cells were collected from old mice. A cell was defined as a grid cell if its grid score exceeded the chance level determined by repeated shuffling of the experimental data (see Methods). In the young mice, 135 cells identified as grid cells were recorded in the MEC. In the old mice, 29 of the MEC grid cells were collected. The fraction of grid cells collected from old mice was significantly lower than that from young mice (Pearson's chi-squared test, $P < 2.2\ 10^{-16}$).

bioRxiv preprint doi: https://doi.org/10.1101/2024.06.27.600930; this version posted July 2, 2024. The copyright holder for this preprint (which was not certified by peer review) is the author/funder, who has granted bioRxiv a license to display the preprint in perpetuity. It is made available under aCC-BY-NC-ND 4.0 International license.

The grid score of the grid cells was significantly lower in old mice than in young mice (young mice: 0.66 ± 0.02, old mice: 0.52 ± 0.02; Kruskal-Wallis test, $P = 1.2 \times 10^{-3}$; Figure 1B, C). However, no difference has been found between the two in their mean firing rate (young mice: 1.36 ± 0.13 Hz; old mice: 1.48 ± 0.31; Kruskal-Wallis test, P = 0.96; Figure 1B). Spatial information of grid cells was significantly lower in old mice than in young mice (young mice: 0.44 ± 0.03; old mice: 0.27 ± 0.05; Kruskal-Wallis test, $P = 2.1 \times 10^{-3}$; Figure 1B). There was also a substantial reduction in the spatial stability of the grid fields in old mice (half-half session stability in young mice: 0.29 ± 0.02; old mice: 0.07 ± 0.02; Kruskal-Wallis test comparing the two sets of correlations, $P = 5.26 \times 10^{-9}$; Figure 1B, C). We also looked into firing stability of some grid cells in two sessions under the same context , and found the cross-session correlation of grid cells in old mice was also significantly lower than that in young mice (young mice: 0.71 ± 0.03; old mice: 0.26 ± 0.05; Kruskal-Wallis test comparing the two sets of correlations, $P = 3.79 \times 10^{-9}$; Figure 1D, E). Although, no change was found between their mean firing rates across different sessions both in young and old mice (young mice, 1st session: 1.82 ± 0.18 Hz, 2nd session: 2.10 ± 0.21 Hz, paired-sample t-test, P = 0.058; old mice, 1st session: 1.42 ± 0.26 Hz, 2nd session: 1.36 ± 0.26 Hz, Paired-sample t-test, P = 0.83; Figure 1F).

Stability of head direction cells but not border cells was impaired in old mice

Considering that spatial navigation also requires information about direction and environmental geometry to accurately reflect the animal´s changing position, we next inquired

bioRxiv preprint doi: https://doi.org/10.1101/2024.06.27.600930; this version posted July 2, 2024. The copyright holder for this preprint (which was not certified by peer review) is the author/funder, who has granted bioRxiv a license to display the preprint in perpetuity. It is made available under aCC-BY-NC-ND 4.0 International license.

if the firing patterns in head direction cells and border cells—recorded simultaneously with grid cells—were affected in old mice. In the young mice group, we identified 95 head direction cells and 25 border cells (see Methods). In the old mouse group, we identified 85 head direction cells and 40 border cells. The fraction of head direction cells in mice was significantly lower than that in young mice (Pearson's chi-square test, $P = 1.9 \times 10^{-3}$). The fraction of border cells was not different between young and old mice (Pearson's chi-square test, P = 0.61).

There were no detectable changes in the directional tuning of head direction cells between the two groups based on mean vector length (young mice: 0.34 ± 0.02; old mice: 0.34 ± 0.02; Kruskal-Wallis test, P = 0.83; Figure 2A-C). A significant increase in the mean firing rates was observed in the head direction cells of old mice (young mice: 0.73 ± 0.10 Hz; old mice: 1.41 ± 0.16; Kruskal-Wallis test, $P = 2.2 \times 10^{-4}$; Figure 2C). Angular stability of head direction cells within sessions was significantly lower in old mice, showing that their head direction cells were unstable (young mice: 0.42 ± 0.03; old mice: 0.32 ± 0.03; Kruskal-Wallis test, P = 0.02; Figure 2C). Moreover, the difference in the cross-session peak direction was significantly larger in old mice, also indicating their head direction cells became unstable across sessions (young mice: 59.29 ± 8.14; old mice: 97.27 ± 11.45; Kruskal-Wallis test, P = $P = 1.82 \times 10^{-3}$; Figure 2A, B, C and Figure S2).

bioRxiv preprint doi: https://doi.org/10.1101/2024.06.27.600930; this version posted July 2, 2024. The copyright holder for this preprint (which was not certified by peer review) is the author/funder, who has granted bioRxiv a license to display the preprint in perpetuity. It is made available under aCC-BY-NC-ND 4.0 International license.

There were no detectable changes in the border scores (young mice: 0.62 ± 0.01; old mice: 0.63 ± 0.01; Kruskal-Wallis test, P = 0.14; Figure 2D-F), mean firing rate (young mice: 1.12 ± 0.35; old mice, 1.42 ± 0.24; Kruskal-Wallis test, P = 0.024; Figure 2F) and spatial information of border cells between young and old mice (young mice: 0.39 ± 0.05; old mice: 0.36 ± 0.05; Kruskal-Wallis test, P = 0.37; Figure 2F). Unlike other cells, we did not find a difference in the stability of border cells between young and old mice in one session (young mice: 0.23 ± 0.04; old mice: 0.18 ± 0.03; Kruskal-Wallis test, P = 0.15; Figure 2F). The stability persisted across different sessions in both young and old mice (Figure S3A). The functional identity of the border cells in old mice was also confirmed by the formation of a new border field after the insertion of a freestanding wall in the recording box (Figure S3B).

Stability of speed-rate relationships of speed cells was reduced in old mice

In our previous study, we found that impaired grid coding after inactivation of parvalbumin (PV) interneurons in the MEC was coupled with disrupted speed coding of speed cells [39]. It is possible that the impairment in the spatial selectivity of the grid cells in the old mice group reflects the impaired integration of speed information from such speed cells. To address this possibility, we examined the tuning of speed in speed cells (see Methods) recorded simultaneously with grid cells. In young mice, 100 cells were classified as speed cells. In old mice, 37 cells were classified as speed cells. The fraction of speed cells collected from old mice was significantly lower than that from young mice (Pearson's chi-squared test, P = 6.54 × 10^{-15}).

bioRxiv preprint doi: https://doi.org/10.1101/2024.06.27.600930; this version posted July 2, 2024. The copyright holder for this preprint (which was not certified by peer review) is the author/funder, who has granted bioRxiv a license to display the preprint in perpetuity. It is made available under aCC-BY-NC-ND 4.0 International license.

Within the speed cell population from young and old mice, there was no significant difference in speed-rate correlations, based on the speed scores (young mice: 0.22 ± 0.01; old mice: 0.21 ± 0.01; Kruskal-Wallis test, P = 0.76; Figure 2G-I). There was no significant difference in the mean firing rates of the speed cells (young mice: 3.32 ± 0.41 Hz; old mice: 4.31 ± 1.41 Hz; Kruskal-Wallis test, P = 0.10; Figure 2I). However, the absolute difference in speed score between the second session and baseline was significantly larger in old mice than in young mice (young mice: 0.09 ± 0.01; old mice: 0.13 ± 0.01 Hz; Kruskal-Wallis test, P = 2.01×10^{-3}; Figure 2I), indicating that the speed-rate relationships in old mice were unstable (Figure 2H).

Theta and Gamma power were decreased in old mice

The spatial periodicity of grid cells is often correlated with theta wave oscillation (6 -12 Hz) [40,41]. To examine whether local field potential (LFP) in MEC alters during aging, we analyzed theta (6 – 12 Hz) and slow gamma (20 – 30 Hz) power of 3 young mice from 187 sessions and 7 old mice from 446 sessions. Old mice exhibited a significant reduction in their theta power (young mice: 48.30 ± 2.34, old mice: 33.85 ± 1.52; Mann-Whitney U-test, P = 7.48×10^{-15}, Figure S4A and S4B), and slow gamma power (young mice: 6.28 ± 0.78, old mice: 6.96 ± 0.49; Mann-Whitney U-test, P = 0.02, Figure S4A and S4B). The data are also presented in the power density spectrum across all frequencies (Figure S4C), indicating impaired LFP power in old mice, especially in theta rhythm which is crucial for grid cell firing.

bioRxiv preprint doi: https://doi.org/10.1101/2024.06.27.600930; this version posted July 2, 2024. The copyright holder for this preprint (which was not certified by peer review) is the author/funder, who has granted bioRxiv a license to display the preprint in perpetuity. It is made available under aCC-BY-NC-ND 4.0 International license.

Gene expression changes during aging are unique in the MEC compared with other brain regions

To examine the gene expression changes in the MEC during aging, we compared the MEC expression patterns between young and old C57BL/6J mice using 10x Genomics Visium technology (Figure 3A). Extensive spatial transcription analyses were performed on 16 sagittal brain sections from the lateral to the middle part of the MEC, using 4 sections per mouse from 2 old mice (> 22 months) and 2 young mice (3- 4 months) (Figures 3B and S5A). This analysis resulted in a total of 50,752 spots (25,493 spots from the young mice group and 25,259 spots from the old mice group) with a median of 5398 genes per spot (Figure S5B). After correcting the batch effect, the uniformity of spatial spots derived from 4 mice was displayed by UMAP in Figure 3C. Within our MEC dataset, a total of 4033 spots (1633 spots from the young mice group and 2400 spots from the old mice group) with 5719 ± 20.16 (Median ± SEM) genes per spot were identified (Figure S5C). To identify differentially expressed genes (DEGs), we compared gene expression patterns between old and young mice. Through these comparisons, we detected 3361 DEGs across the entire brain sections and 1664 DEGs in the MEC during aging. (Table S1). The Venn diagram showed the number of DEGs detected in the MEC, the entire brain, or both, with 479 DEGs shown as differentially expressed during aging in the MEC only (Figure 3D). We also conducted bulk-seq on MEC of 3 old and 3 young C57BL/6J mice and there were 573 DEGs consistent with 10x visium data (Figure S5D, S5E and Table S2). 50 down-regulated and up-regulated genes within the

bioRxiv preprint doi: https://doi.org/10.1101/2024.06.27.600930; this version posted July 2, 2024. The copyright holder for this preprint (which was not certified by peer review) is the author/funder, who has granted bioRxiv a license to display the preprint in perpetuity. It is made available under aCC-BY-NC-ND 4.0 International license.

MEC during aging are shown in Figure 3E, and the expression of 28 of these DEGs (8 upregulated and 20 downregulated in old mice) was verified using reverse transcription quantitative PCR (RT-qPCR) (Figure S6). The genes that were upregulated in old mice are highly protective genes. For example, *Sgk1* and *ApoD* maintain nerve integrity and rescue the neural cytoskeleton [42,43], and *Bhlhe40* is a transcriptional regulator that enhances synaptic plasticity [44]. Among the genes that were downregulated in old mice, some genes such as *Tubb2b, Neto1 and Calb2*, have been associated with cognitive deficits [45–47], and mutation or knockdown of these genes resulted in impaired long-term potentiation and neural excitability.

Furthermore, we performed GO enrichment analysis on 1664 DEGs (754 up and 910 downregulated DEGs) (Figure 3F). We found elevated signaling pathways including immune and oxidative stress response, which indicates imbalance and cumulated damage happening to the central nervous system during aging [48]. In addition, signaling related to the positive regulation of cell/neural death and apoptosis was upregulated in the MEC of old mice. In contrast, signaling related to extracellular matrix organization, cell morphogenesis and cell junction organization was downregulated in the MEC of old mice, suggesting that the dysfunction of these signaling pathways is likely related to the impaired function of the MEC during aging.

bioRxiv preprint doi: https://doi.org/10.1101/2024.06.27.600930; this version posted July 2, 2024. The copyright holder for this preprint (which was not certified by peer review) is the author/funder, who has granted bioRxiv a license to display the preprint in perpetuity. It is made available under aCC-BY-NC-ND 4.0 International license.

To examine the changes in gene expression across the different MEC layers, we delineated the MEC into superficial (MEC_s), intermediate (MEC_im) and deep (MEC_d) layers based on the anatomical structure from hematoxylin and eosin (H&E) staining (Figure 3G, H and S7A). UMAP dimensional reduction on spots selected from old and young mice MEC regions showed three continuous sequential MEC sublayer clusters (Figure 3I and S7B). We plotted several known MEC marker genes such as *Calb1* and *Reln* (MEC layer II marker genes), *Oxr1* (MEC layer III maker gene) and *Cux2* (upper cortical layer marker) based on previous *in vivo* functional studies [49–52], along with several other MEC deep layer marker genes (*Plch1, Rmst, Cplx3* and *Cobll1*) that were discussed in previous scRNA-seq studies to validate the accuracy of our method [31,53] (Figure S7C). Then we compared gene expression levels between old and young mice in three MEC layers and discovered 166, 1108 and 5 layer-specific DEGs between old and young mice. We also identified 31 genes that exhibited differential expression across all three layers, along with 297 genes common to MEC_s and MEC_im layers, and 37 genes shared between MEC_im and MEC_d layers (Figure 3J and Table S3). By specifying the MEC subregion, we found DEGs that were not discovered previously in our whole MEC DEGs lists (gene names were highlighted in red, Figure 3K), indicating the unique changes happening in MEC sublayers during aging, which helps us to have further understanding of the molecular changes in MEC while aging.

Bglap3+ neurons are critical for spatial coding of the MEC

bioRxiv preprint doi: https://doi.org/10.1101/2024.06.27.600930; this version posted July 2, 2024. The copyright holder for this preprint (which was not certified by peer review) is the author/funder, who has granted bioRxiv a license to display the preprint in perpetuity. It is made available under aCC-BY-NC-ND 4.0 International license.

Through the 10x Genomics Visium experiment, we identified the gene *Bglap3* that was specifically expressed in the MEC (Figure 3F, L and 4A). Number of spots that were detected with Bglap3 was significantly lower in MEC of old mice (young mice: 68.36 ± 19.80; old mice: 30.58 ± 2.72; Mann–Whitney U-test, P = 2× 10^{-4}; Figure 4B). Our *in situ* hybridization (ISH) results further confirmed that *Bglap3* expression was unique to the MEC (Figure 4C, D), *Bglap3* ISH signal was specifically confined to the NeuN+ cells in the MEC (Figure 4E, F) and the percentage of MEC cells expressing *Bglap3* were significantly decreased in old mice (young mice: 48.71 ± 3.11%; old mice: 37.51 ± 3.01%; Mann–Whitney U-test, P = 0.0232; Figure 4G, H). This demonstrated that *Bglap3*+ neurons were specifically localized in the MEC and that their numbers decreased during aging, implying a potential relationship between aging-related changes in *Bglap3*+ neurons and MEC dysfunction.

To further investigate the function of *Bglap3*+ neurons, we built a *Bglap3-Cre* gene knock-in mouse line (Figure S9A). ISH showed co-localization of *Bglap3* with *Cre* (Figure S9B and S9C). Moreover, Cre-driven reporter fluorescence protein expression was only present in the MEC rather than the cortex region (Figure S9D), confirming the validity of the *Bglap3-Cre* mice. We also injected AAV carrying DIO-mCherry into MEC of *Bglap3-Cre* mice and co-stained the brain slices with NeuN and GAD67 to see Bglap3 expression in excitatory and inhibitory neuronal populations. The results showed that only 0.1% of NeuN+ cells expressed both *Bglap3-Cre* driven mCherry and GAD67, excluding the possibility of inhibitory neurons expressing *Bglap3* (Figure S9E and S9F). By assuring *Bglap3* was expressed in excitatory

bioRxiv preprint doi: https://doi.org/10.1101/2024.06.27.600930; this version posted July 2, 2024. The copyright holder for this preprint (which was not certified by peer review) is the author/funder, who has granted bioRxiv a license to display the preprint in perpetuity. It is made available under aCC-BY-NC-ND 4.0 International license.

neurons, we then injected AAV2/9-hSyn-DIO-Synaptophysin-EGFP in the MEC of the *Bglap3-Cre* mice to label the axon terminal of the *Bglap3*+ neurons (Figure 4I). Our data showed that the *Bglap3*+ neurons mainly project to the ipsi- and contralateral hippocampus, subiculum, and MEC (Figure 4J). Next, we labeled *Bglap3*+ cells with Cre-dependent TVA and G proteins (injecting AAV2/8-DIO-EGFP-TVA and AAV2/8-DIO-oRVG) following rabies virus injection (EnvA-RVdG-mCherry) in the MEC of the *Bglap3-Cre* mice (Figure 4K). Rabies virus that was injected in the MEC initiated the retrograde labeling of the presynaptic network of *Bglap3*+ cells (Figure 4L). We found that the presynaptic neurons that project to the *Bglap3*+ neurons were mainly localized in the ipsilateral MEC, parasubiculum, postsubiculum, and subiculum; and only sparsely found in the hippocampus, retrosplenial cortex and contralateral MEC (Figure 4M). There was a higher probability of recurrent connection among neurons revealed by presynaptic cells that are located in superficial of MEC (Figure 4N).

To investigate *in vivo* function of *Bglap3*+ cells and their role in MEC microcircuit, we conducted two-photon calcium imaging using a miniaturized Two-Photon Microscope (TPM) according to recently published methods [54]. For imaging *in vivo* firing activity of *Bglap3*+ cell and overall MEC spatial cells while chemogenetically silencing *Bglap3*+ cells, we injected either AAV2/9-GCaMP6s alone or a mixture of AAV2/9-DIO-hM4D-mCherry with AAV2/9-GCaMP6s in the right MEC of *Bglap3-Cre* mice (Figure 5A, B, S10A and S10B). All mice showed average trajectory coverage above 90% and no anxiety-related behavior was detected in 5 sessions (Figure S11B-H). By imaging *Bglap3* positive cells tagged with Cre-

bioRxiv preprint doi: https://doi.org/10.1101/2024.06.27.600930; this version posted July 2, 2024. The copyright holder for this preprint (which was not certified by peer review) is the author/funder, who has granted bioRxiv a license to display the preprint in perpetuity. It is made available under aCC-BY-NC-ND 4.0 International license.

dependent GCaMP6s or aligning mCherry-expressing *Bglap3*+ cells with GCaMP6s-expressing cells (see Methods; Figure 5C and 5D), we found 132 *Bglap3* positive (*Bglap3*+) and 669 *Bglap3* negative (*Bglap3*-) neurons. Among *Bglap3*+ or *Bglap3*- neurons, there were mixed populations of spatial cells, including 3.72% or 12.72% grid cells, 8.44% or 9.18% border cells, 20.39% or 16.12% head direction cells, and 11.77% and 16.13% unclassified spatial cells. Percentages of different spatial cells among *Bglap3*+ and *Bglap3*- neurons did not exhibit significant difference except for gird cell population which showed a decreased population in *Bglap3*+ neurons (*Bglap3*+ cells vs. *Bglap3*- cells; grid cells: $P = 0.0052$, border cells: $P = 0.9164$, head direction cells: $P = 0.2837$, spatial cells: $P = 0.2555$; Pearson's chi-squared test; Figure 5E and 5F). Cell type definition was restricted only to those cells that were stable between two baseline sessions (see Methods). *Bglap3* positive and negative grid cells displayed no difference in their grid scores during two baseline sessions (Figure S12A), the same as *Bglap3* positive and negative head direction cells on their correlations of directional tuning curves (Figure S12B). There were also no differences between *Bglap3* positive and negative spatial tuning cells (SPT) in their spatial information contents, however, *Bglap3* negative spatial tuning cells showed a higher correlation of rate maps across baseline sessions than *Bglap3* positive cells (Figure S12C). After DCZ injection, the mean firing rate of *Bglap3*+ cells was significantly decreased (BL 1 vs. DCZ: $q < 0.001$, BL 2 vs. DCZ: $q = 0.0041$, One-way ANOVA; Figure 5G, S12D and S12E), indicating that the inactivation of *Bglap3*+ cells was successful. After 24 hours, the mean firing rate recovered to at least the baseline level before DCZ injection (RC 1 vs. BL 2: $q = 0.1608$, RC 2 vs. BL 2: $q = 0.2857$,

bioRxiv preprint doi: https://doi.org/10.1101/2024.06.27.600930; this version posted July 2, 2024. The copyright holder for this preprint (which was not certified by peer review) is the author/funder, who has granted bioRxiv a license to display the preprint in perpetuity. It is made available under aCC-BY-NC-ND 4.0 International license.

RC1 vs. DCZ: q = 0.0007, RC 2 vs. DCZ: q = 0.0048, One-way ANOVA). When selectively inactivating *Bglap3*+ neurons, we noticed a decrease in the mean firing rate among *Bglap3*- negative cells (Figure S12F, G). This was further confirmed histologically that c-Fos intensity reduced with DCZ injection in both *Bglap3* positive and negative cell populations (Figure S12H, I and J). By further characterizing the firing properties of each cell type among *Bglap3*- negative cells after silencing of *Bglap3*+ neurons, we observed a significant decrease in the grid scores of those *Bglap3*- grid cells (BL1 vs. DCZ: P = 0.0013, BL 2 vs. DCZ: P < 0.0001, One-way ANOVA; Figure 5H). The grid scores remained consistent between the two 40-minute baseline sessions (BL1 vs. BL2: P > 0.9999, One-way ANOVA; Figure 5H), indicating that the observed decrease was not a result of temporal drift. In terms of firing rate maps and autocorrelograms, the regular hexagonally arranged firing fields of the grid cells were impaired. Certain grids disappeared or exhibited irregularity after DCZ injection (see the example cells in Figure 5I and S13A) leading to significant drops in the correlation of firing rate maps between the DCZ and baseline sessions (Figure S13B). There was no difference in spatial information of the *Bglap3*- grid cells (BL1 vs. DCZ: P = 0.9260, BL2 vs. DCZ: P > 0.9999, BL1 vs. BL2: P = 0.5279, RC1 vs. DCZ: P > 0.9999, RC2 vs. DCZ: P > 0.9999, One-way ANOVA; Figure 5J). Following DCZ injection, the mean vector length of the *Bglap3*- head direction cells decreased (BL1 vs. DCZ: q = 0.0083, BL2 vs. DCZ: q < 0.0001, RC1 vs. DCZ: q = 0.0005, RC2 vs. DCZ: q = 0.1758, One-way ANOVA; Figure 5K, 5L and S12C; BL1 vs. DCZ: q = 0.0107, BL2 vs. DCZ: q < 0.0001, RC1 vs. DCZ: q = 0.0008, RC2 vs. DCZ: q = 0.2110, One-way ANOVA; Figure 5M), and the dispersion around their preferred direction

bioRxiv preprint doi: https://doi.org/10.1101/2024.06.27.600930; this version posted July 2, 2024. The copyright holder for this preprint (which was not certified by peer review) is the author/funder, who has granted bioRxiv a license to display the preprint in perpetuity. It is made available under aCC-BY-NC-ND 4.0 International license.

increased (Figure S13D). These findings indicated a decline in the directional selectivity of the *Bglap3*- head direction cells. For the *Bglap3*- border cells, the firing event locations became more chaotic with less boundary selectivity. Predictably, this phenomenon resulted in a significant decrease in border scores (BL1 vs. DCZ: q = 0.0001, BL2 vs. DCZ: q = 0.0096, RC1 vs. DCZ: q = 0.3603, RC2 vs. DCZ: q = 0.4103, One-way ANOVA; Figure 5N, O and S13E). The spatial information of *Bglap3*- border cells was also decreased when compared with the baseline session (BL1 vs. DCZ: q = 0.1442, BL2 vs. DCZ: q = 0.0101, RC1 vs. DCZ: q = 0.2114, RC2 vs. DCZ: q = 0.2035, One-way ANOVA; Figure 5P). No change was found in the spatial information content of *Bglap3*- spatial cells (Figure S13F and G). However, rate map correlation of *Bglap3*- spatial cells was decreased after DCZ injection (Figure S13H). Collectively, these data suggest a pivotal function of *Bglap3*+ neurons in the spatial circuits of the MEC, and that changes in these neurons may relate to the impaired spatial cognition that occurs during aging.

In order to examine the role of *Bglap3*+ cells in spatial learning, we conducted water maze training with 20 young mice, 12 of which were injected with deschloroclozapine (DCZ) to silence Bglap3+ cells expressing hM4D and the rest were injected with saline as control group (Figure 6A and B). The water maze learning task comprised three distinct paradigms: the ‘Train’ session, in which mice learned the platform’s location under normal lighting conditions with four different cues surrounding the circular maze (Figure 6C and S14A); the ‘New location’ session, in which the platform’s position was switched to the opposite quadrant of

bioRxiv preprint doi: https://doi.org/10.1101/2024.06.27.600930; this version posted July 2, 2024. The copyright holder for this preprint (which was not certified by peer review) is the author/funder, who has granted bioRxiv a license to display the preprint in perpetuity. It is made available under aCC-BY-NC-ND 4.0 International license.

the circular maze (Figure 6D and S14B); and the 'Dark' session, in which the lights were turned off, requiring the mice to find the platform using path-integration without surrounding cues (Figure 6E and S14C). We evaluated mice performance based on the distance traveled to reach the platform location. The DCZ group did not exhibit a significant difference compared to the Saline group during the 'Train' sessions (Figures 6B and S14A). However, in the 'New location' session, when the platform was relocated to a new position, the DCZ group showed impaired spatial performance on Day 3 and Day 4 (Day 3: DCZ vs. Saline, P = 0.0447; Day 4: DCZ vs. Saline, P = 0.0320, Multiple t-tests, Figures 6B and S14B). A similar impairment was also observed during the 'Dark' path integration learning (Day 2: DCZ vs. Saline, P = 0.0152; Day 3: DCZ vs. Saline, P = 0.0482, Multiple t-tests, Figures 6B and S14C). Importantly, there was no overall difference in swimming velocity between the DCZ and Saline groups in all three paradigms (Figure S14A-C). These data suggested a potential function of *Bglap3*+ cells in spatial coding during navigation.

Discussion

In this study, we found that few grid cells in old mice compared with young mice's. Reduced grid score in old mice was associated with less consistent coding across sessions. Head direction cells and speed cells exhibited reduced stability in old mice but not border cells. Through gene expression analysis, we identified candidate biological processes related to impaired MEC function during aging and discovered a population of cells located at MEC Layer III that express the *Bglap3*, with a significantly decreased number in old mice.

bioRxiv preprint doi: https://doi.org/10.1101/2024.06.27.600930; this version posted July 2, 2024. The copyright holder for this preprint (which was not certified by peer review) is the author/funder, who has granted bioRxiv a license to display the preprint in perpetuity. It is made available under aCC-BY-NC-ND 4.0 International license.

Selectively labeling and inactivating *Bglap3*+ neurons disrupted the tuning of spatial cells. In a water maze task, inhibition of *Bglap3*+ neurons impaired mice performance during the platform relocation and dark sessions, indicating the important role of *Bglap3*+ cells in spatial learning and their potential impact on the unstable firing of spatial cells during aging.

Spatial learning and memory are dramatically impaired during aging among numerous species [1,2], which may be caused by impaired function of the MEC and hippocampus. To exclude the possibility that impaired vision affected the navigation of old mice, we trained them in a visual cue discrimination test and found that the old mice did not exhibit a significant decline in their performance (young v.s. old: Stage 1, P = 0.9710; Stage 2, P = 0.8420; Stage 3, P = 0.9995; Stage 4, P = 0.7730; Stage 5, P = 0.9460; Bonferroni and Sidak multiple comparisons; Figure S15A and S15B). Therefore the vision capacity was intact in old mice in our experiment.

Grid cells, as key components of the MEC circuit, play an essential role in spatial computation and memory [9]. The unstable firing of grid cells in old mice could be related to the navigation deficiency that occurs during aging because inaccurate grid coding could cause errors in path integration and impair spatial computation [14]. Our LFP recordings revealed a significant decrease in theta and slow gamma power in old mice indicating a network-level changes in old mice MEC that is correlated with irregular firings of grid cells. We have not seen the difference between the running speed of freely behaving young and old mice in our

bioRxiv preprint doi: https://doi.org/10.1101/2024.06.27.600930; this version posted July 2, 2024. The copyright holder for this preprint (which was not certified by peer review) is the author/funder, who has granted bioRxiv a license to display the preprint in perpetuity. It is made available under aCC-BY-NC-ND 4.0 International license.

recordings, thus excluding the possibility of reduction in theta power due to lower running speed. In previous studies, inactivation of medial septum (MS) reduced theta rhythm and disrupted grid firing in MEC [40,41]. Although we could not exclude the possibility of neuronal loss and other chronic changes in aged MS that eventually impacted grid firing in aging MEC [55,56], our observation on unstable firing of other spatial coding cells such as head direction cells and speed cells that often are not impacted by theta rhythms, support the conclusion that local changes happening in MEC during aging, including grid cells. The reduction in slow gamma power in aging MEC provides evidence of unstable coding of place cells in the hippocampus in aged rodents [57], since coordination of gamma between MEC and hippocampus is crucial for memory coding and retrieval [58]. It would be interesting to understand whether the aging-related changes in grid cells occurred earlier than the changes in place cells or vice versa, and whether the changes in theta and gamma bands take part in similar outcomes that are discovered in grid cells and place cell populations during aging. Overall, it is likely that the changes in spatial representation occurring in the hippocampus and MEC, including the instability of place cells and grid cells, are the major reasons for the reduced spatial learning and memory in old age.

However, unlike other spatial coding cells in MEC, border cells in old mice did not show unstable firing within or across sessions (Figure 2E and S3B). During development, border cells show adult-like fields from the outset whereas grid cells show irregular firing until 4-week-old [59,60]. A clearer representation of borders is more dependent on tactile and visual

bioRxiv preprint doi: https://doi.org/10.1101/2024.06.27.600930; this version posted July 2, 2024. The copyright holder for this preprint (which was not certified by peer review) is the author/funder, who has granted bioRxiv a license to display the preprint in perpetuity. It is made available under aCC-BY-NC-ND 4.0 International license.

input, rather than speed, and idiothetic input that grid cells and head direction cells require for path- or angular-path integration [61,62], which might help us to understand border cells being less vulnerable to aging than other spatial coding cells in MEC.

Grid cell coding is influenced by various factors, and changes in external inputs can affect the computation of the grid cells [63]. Impaired grid coding may also result from local changes inside the MEC, as many signaling pathways were changed in the MEC during aging (Figure 3G). Multiple changes at the structural, molecular, and cellular levels have been identified in the neurons of old animals [64]. In older animals, long-term potentiation (LTP) is difficult to induce and can easily decay [65,66], whereas long-term depression (LTD) can be activated normally [66]. This observation is consistent with our gene expression data in old mice, which showed decreased expression of several genes, such as *Tubb2b, Neto1* and *Calb2*; furthermore, the mutation or knockdown of these genes has resulted in impaired LTP and neural excitability [45–47]. The instability we observed in the grid cells of old mice (Figure 1B–F) could be caused by the decline in LTP during aging because changes in the balance between LTP and LTD could cause impairments in consolidation of spatial memory and inaccuracies in spatial coding. This imbalance could also lead to accumulated errors in navigation due to the dysfunction in path integration, which is impaired during aging [67,68].

Aged transgenic mice expressing mutant human tau in the entorhinal cortex have been found to have impairments in grid coding as well as spatial memory [27]. In addition, young human

bioRxiv preprint doi: https://doi.org/10.1101/2024.06.27.600930; this version posted July 2, 2024. The copyright holder for this preprint (which was not certified by peer review) is the author/funder, who has granted bioRxiv a license to display the preprint in perpetuity. It is made available under aCC-BY-NC-ND 4.0 International license.

adults at risk for developing AD, who carry the APOE-ε4 allele, exhibit impaired grid cell-like activity in the MEC [28]. These studies have raised the possibility of including grid cells in the early diagnosis of AD. In our study, we examined changes in gene expression during aging using 10x Genomics Visium technology. We did not find notable changes in the expression of AD-related genes in the entorhinal cortex—which were previously reported in a study of AD patients[69]—indicating that the changes in grid coding in our system were not likely caused by AD-related symptoms. Our data support the possibility that changes in grid cells will occur during normal aging regardless of the development of AD, which is consistent with the results from healthy older humans [26].

In our gene expression analysis, we found the DEGs that were upregulated in old mice, most of them were related to cell injury and cell death, which is consistent with earlier reports [64]. In contrast, the downregulated DEGs were related to neural development and circuit maturation, indicating impaired homeostasis in the neural circuits of old mice. One of these DEGs, *Bglap3*, exhibited selective expression in layer III of MEC and decreased cell number during aging. Our data with the *Bglap3*+ population in layer III of the MEC provide a potential role of MEC layer III in aging.

In our axon tagging studies, we found *Bglap3*+ neurons project to ipsi/contralateral MEC superficial layer, subiculum and hippocampus, which is consistent with previous histology studies done on MEC layer III neurons [51,70–72]. However, few studies have been done on

bioRxiv preprint doi: https://doi.org/10.1101/2024.06.27.600930; this version posted July 2, 2024. The copyright holder for this preprint (which was not certified by peer review) is the author/funder, who has granted bioRxiv a license to display the preprint in perpetuity. It is made available under aCC-BY-NC-ND 4.0 International license.

upstream projections to MEC layer III [73]. In our rabies virus tracing experiment, *Bglap3*+ neurons receive their upstream inputs from ipsilateral MEC and several other parahippocampal regions such as parasubiculum, and postsubiculum. Albeit the insufficient labeling of starter cells (n = 32) which could bias our observations, it described possible upstream brain regions that might help us to study the information *Bglap3*+ neurons encode. Our data also supports recurrent connection in MEC superficial layers which was believed to be crucial for head directions cells and grid cells in forming attractor networks [74–77]. *In vivo* electrophysiological results show that most third-layer cells in the MEC are non-spatial cells and spatially irregular cells, with a smaller percentage of grid cells [70], which is consistent with our findings in *Bglap3*+ neurons (Figure 5F). Our combined chemogenetic silencing and calcium imaging study revealed that inactivating the *Bglap3*+ neurons caused an irregular firing of grid cells and a decrease in the precise directional tuning of head direction cells and border tuning of border cells, which indicates *Bglap3*+ cells have a special modulatory function in the local spatial network of MEC. *In vitro* electrophysiological studies have found that third-layer cells in the MEC project more commonly to layer II stellate cells than to layer II pyramidal cells and that the second-layer MEC has the highest number of grid cells [78]. Our calcium imaging data provided *in vivo* evidence on layer III *Bglap3*+ neurons' potential connections with MEC spatial cells, especially grid cells which are most likely to be located in layer II of MEC [79]. By combining our behavioral and physiology data, we found the decreased performance in water maze after the inactivation of *Bglap3*+ cells might relate to irregular firing of spatial cells inside the MEC. In fact, previous research has proven the

bioRxiv preprint doi: https://doi.org/10.1101/2024.06.27.600930; this version posted July 2, 2024. The copyright holder for this preprint (which was not certified by peer review) is the author/funder, who has granted bioRxiv a license to display the preprint in perpetuity. It is made available under aCC-BY-NC-ND 4.0 International license.

correlation between impaired grid firing and performance in path-integration–dependent water maze [14]. Consistent with these results, we found a decreased performance in water maze after inactivation of *Bglap3*+ cells, implying the contribution of *Bglap3*+ cells in path-integration. With population decrease found in *Bglap3*+ neurons during aging, it would be important to rule out whether irregular and instable tunings of grid cells in aged mice are due to the loss of *Bglap3*+ neurons. Furthurmore, *Bglap3*+ neurons also send projections to hippocampus CA1, the latter contains place cells that also become instable during aging, it would to necessary to see how *Bglap3*+ neurons influence place cells. In future studies, it would be necessary to examine the function of Bglap3 protein in MEC microcircuit with more detailed mechanisms that modulates *Bglap3*+ cells during aging.

Acknowledgments

We thank Jialing Zhao and Julien Rousseau for proofreading the manuscript. This work was supported by the National Key R&D Program of China (2019YFA0802400), the Lingang Laboratory, Grant No. LG-TKN-202204-01, the State Key Laboratory of Membrane Biology (open project for Chenglin Miao), and the Qidong-SLS Innovation Fund (Grant No. 2023002029 and 2020001540). We thank the Core Facilities of the School of Life Sciences, the State Key Laboratory of Membrane Biology at Peking University for assistance with confocal microscopy and Miniaturized Two-Photon Microscope.

Author contributions

bioRxiv preprint doi: https://doi.org/10.1101/2024.06.27.600930; this version posted July 2, 2024. The copyright holder for this preprint (which was not certified by peer review) is the author/funder, who has granted bioRxiv a license to display the preprint in perpetuity. It is made available under aCC-BY-NC-ND 4.0 International license.

Q.C. and C.M. planned and designed the initial experiments, with later input from S.U.. Q.C. and C.M. collected and analyzed the tetrode recording data. S.U., S.C., and J.L. performed 10x Genomics Visium experiments and analyzed the data. Y.L., S.W., J.H., X.Y., and M.Z. performed surgeries and collected the calcium imaging data. Y.L. analyzed the calcium imaging data. S.U. performed and analyzed histology data. S.U. and S.C. performed behavioral experiments and analyzed the data. Y.Y. and S.Y. provided code for behavior analysis. W.G. provided the rabies for tracing. C.M. supervised the project and provided funding. S.U. and Y.L. made the figures. S.U. and C.M. wrote the manuscript with input from all authors.

Declaration of interests

The authors declare no competing interests.

References

1. Moffat, S.D. (2009). Aging and spatial navigation: what do we know and where do we go? Neuropsychol Rev *19*, 478–489. 10.1007/s11065-009-9120-3.
2. Lester, A.W., Moffat, S.D., Wiener, J.M., Barnes, C.A., and Wolbers, T. (2017). The Aging Navigational System. Neuron *95*, 1019–1035. 10.1016/j.neuron.2017.06.037.
3. Moffat, S.D., Zonderman, A.B., and Resnick, S.M. (2001). Age differences in spatial memory in a virtual environment navigation task. Neurobiol Aging *22*, 787–796. 10.1016/s0197-4580(01)00251-2.
4. Burns, P.C. (1999). Navigation and the mobility of older drivers. J Gerontol B Psychol Sci Soc Sci *54*, S49-55. 10.1093/geronb/54b.1.s49.
5. Rapp, P.R., Kansky, M.T., and Roberts, J.A. (1997). Impaired spatial information processing in aged monkeys with preserved recognition memory. Neuroreport *8*, 1923–1928. 10.1097/00001756-199705260-00026.

bioRxiv preprint doi: https://doi.org/10.1101/2024.06.27.600930; this version posted July 2, 2024. The copyright holder for this preprint (which was not certified by peer review) is the author/funder, who has granted bioRxiv a license to display the preprint in perpetuity. It is made available under aCC-BY-NC-ND 4.0 International license.

6. Head, E., Mehta, R., Hartley, J., Kameka, M., Cummings, B.J., Cotman, C.W., Ruehl, W.W., and Milgram, N.W. (1995). Spatial learning and memory as a function of age in the dog. Behav Neurosci *109*, 851–858. 10.1037//0735-7044.109.5.851.
7. Barnes, C.A. (1979). Memory deficits associated with senescence: a neurophysiological and behavioral study in the rat. J Comp Physiol Psychol *93*, 74–104. 10.1037/h0077579.
8. Bach, M.E., Barad, M., Son, H., Zhuo, M., Lu, Y.F., Shih, R., Mansuy, I., Hawkins, R.D., and Kandel, E.R. (1999). Age-related defects in spatial memory are correlated with defects in the late phase of hippocampal long-term potentiation in vitro and are attenuated by drugs that enhance the cAMP signaling pathway. Proc Natl Acad Sci U S A *96*, 5280–5285. 10.1073/pnas.96.9.5280.
9. Moser, M.-B., Rowland, D.C., and Moser, E.I. (2015). Place Cells, Grid Cells, and Memory. Cold Spring Harb Perspect Biol *7*, a021808. 10.1101/cshperspect.a021808.
10. Rowland, D.C., Roudi, Y., Moser, M.-B., and Moser, E.I. (2016). Ten Years of Grid Cells. Annu Rev Neurosci *39*, 19–40. 10.1146/annurev-neuro-070815-013824.
11. Stranahan, A.M., and Mattson, M.P. (2010). Selective vulnerability of neurons in layer II of the entorhinal cortex during aging and Alzheimer's disease. Neural Plast *2010*, 108190. 10.1155/2010/108190.
12. Scharfman, H.E., and Chao, M.V. (2013). The entorhinal cortex and neurotrophin signaling in Alzheimer's disease and other disorders. Cognitive Neuroscience *4*, 123–135. 10.1080/17588928.2013.826184.
13. Steffenach, H.-A., Witter, M., Moser, M.-B., and Moser, E.I. (2005). Spatial memory in the rat requires the dorsolateral band of the entorhinal cortex. Neuron *45*, 301–313. 10.1016/j.neuron.2004.12.044.
14. Gil, M., Ancau, M., Schlesiger, M.I., Neitz, A., Allen, K., De Marco, R.J., and Monyer, H. (2018). Impaired path integration in mice with disrupted grid cell firing. Nat Neurosci *21*, 81–91. 10.1038/s41593-017-0039-3.
15. Hafting, T., Fyhn, M., Molden, S., Moser, M.-B., and Moser, E.I. (2005). Microstructure of a spatial map in the entorhinal cortex. Nature *436*, 801–806. 10.1038/nature03721.
16. Sargolini, F., Fyhn, M., Hafting, T., McNaughton, B.L., Witter, M.P., Moser, M.-B., and Moser, E.I. (2006). Conjunctive Representation of Position, Direction, and Velocity in Entorhinal Cortex. Science *312*, 758–762. 10.1126/science.1125572.
17. Savelli, F., Yoganarasimha, D., and Knierim, J.J. (2008). Influence of boundary removal on the spatial representations of the medial entorhinal cortex. Hippocampus *18*, 1270–1282. 10.1002/hipo.20511.
18. Solstad, T., Boccara, C.N., Kropff, E., Moser, M.-B., and Moser, E.I. (2008). Representation of geometric borders in the entorhinal cortex. Science *322*, 1865–1868. 10.1126/science.1166466.
19. Kropff, E., Carmichael, J.E., Moser, M.-B., and Moser, E.I. (2015). Speed cells in the medial entorhinal cortex. Nature *523*, 419–424. 10.1038/nature14622.
20. Hinman, J.R., Brandon, M.P., Climer, J.R., Chapman, G.W., and Hasselmo, M.E. (2016). Multiple Running Speed Signals in Medial Entorhinal Cortex. Neuron *91*, 666–679. 10.1016/j.neuron.2016.06.027.
21. Deshmukh, S.S., and Knierim, J.J. (2011). Representation of non-spatial and spatial information in the lateral entorhinal cortex. Front Behav Neurosci *5*, 69. 10.3389/fnbeh.2011.00069.

bioRxiv preprint doi: https://doi.org/10.1101/2024.06.27.600930; this version posted July 2, 2024. The copyright holder for this preprint (which was not certified by peer review) is the author/funder, who has granted bioRxiv a license to display the preprint in perpetuity. It is made available under aCC-BY-NC-ND 4.0 International license.

22. Tsao, A., Moser, M.-B., and Moser, E.I. (2013). Traces of experience in the lateral entorhinal cortex. Curr Biol *23*, 399–405. 10.1016/j.cub.2013.01.036.
23. O'Keefe, J., and Dostrovsky, J. (1971). The hippocampus as a spatial map. Preliminary evidence from unit activity in the freely-moving rat. Brain Res *34*, 171–175. 10.1016/0006-8993(71)90358-1.
24. Eichenbaum, H., Kuperstein, M., Fagan, A., and Nagode, J. (1987). Cue-sampling and goal-approach correlates of hippocampal unit activity in rats performing an odor-discrimination task. J Neurosci *7*, 716–732. 10.1523/JNEUROSCI.07-03-00716.1987.
25. Sarel, A., Finkelstein, A., Las, L., and Ulanovsky, N. (2017). Vectorial representation of spatial goals in the hippocampus of bats. Science *355*, 176–180. 10.1126/science.aak9589.
26. Stangl, M., Achtzehn, J., Huber, K., Dietrich, C., Tempelmann, C., and Wolbers, T. (2018). Compromised Grid-Cell-like Representations in Old Age as a Key Mechanism to Explain Age-Related Navigational Deficits. Curr Biol *28*, 1108-1115.e6. 10.1016/j.cub.2018.02.038.
27. Fu, H., Rodriguez, G.A., Herman, M., Emrani, S., Nahmani, E., Barrett, G., Figueroa, H.Y., Goldberg, E., Hussaini, S.A., and Duff, K.E. (2017). Tau Pathology Induces Excitatory Neuron Loss, Grid Cell Dysfunction, and Spatial Memory Deficits Reminiscent of Early Alzheimer's Disease. Neuron *93*, 533-541.e5. 10.1016/j.neuron.2016.12.023.
28. Kunz, L., Schröder, T.N., Lee, H., Montag, C., Lachmann, B., Sariyska, R., Reuter, M., Stirnberg, R., Stöcker, T., Messing-Floeter, P.C., et al. (2015). Reduced grid-cell-like representations in adults at genetic risk for Alzheimer's disease. Science *350*, 430–433. 10.1126/science.aac8128.
29. Merrill, D.A., Chiba, A.A., and Tuszynski, M.H. (2001). Conservation of neuronal number and size in the entorhinal cortex of behaviorally characterized aged rats. J. Comp. Neurol. *438*, 445–456. 10.1002/cne.1327.
30. Tasic, B., Menon, V., Nguyen, T.N., Kim, T.K., Jarsky, T., Yao, Z., Levi, B., Gray, L.T., Sorensen, S.A., Dolbeare, T., et al. (2016). Adult mouse cortical cell taxonomy revealed by single cell transcriptomics. Nat Neurosci *19*, 335–346. 10.1038/nn.4216.
31. Yao, Z., Van Velthoven, C.T.J., Nguyen, T.N., Goldy, J., Sedeno-Cortes, A.E., Baftizadeh, F., Bertagnolli, D., Casper, T., Chiang, M., Crichton, K., et al. (2021). A taxonomy of transcriptomic cell types across the isocortex and hippocampal formation. Cell *184*, 3222-3241.e26. 10.1016/j.cell.2021.04.021.
32. Boisvert, M.M., Erikson, G.A., Shokhirev, M.N., and Allen, N.J. (2018). The Aging Astrocyte Transcriptome from Multiple Regions of the Mouse Brain. Cell Reports *22*, 269–285. 10.1016/j.celrep.2017.12.039.
33. Ximerakis, M., Lipnick, S.L., Innes, B.T., Simmons, S.K., Adiconis, X., Dionne, D., Mayweather, B.A., Nguyen, L., Niziolek, Z., Ozek, C., et al. (2019). Single-cell transcriptomic profiling of the aging mouse brain. Nat Neurosci *22*, 1696–1708. 10.1038/s41593-019-0491-3.
34. Macosko, E.Z., Basu, A., Satija, R., Nemesh, J., Shekhar, K., Goldman, M., Tirosh, I., Bialas, A.R., Kamitaki, N., Martersteck, E.M., et al. (2015). Highly Parallel Genome-wide Expression Profiling of Individual Cells Using Nanoliter Droplets. Cell *161*, 1202–1214. 10.1016/j.cell.2015.05.002.
35. Chen, A., Liao, S., Cheng, M., Ma, K., Wu, L., Lai, Y., Qiu, X., Yang, J., Xu, J., Hao, S., et al. (2022). Spatiotemporal transcriptomic atlas of mouse organogenesis using DNA nanoball-patterned arrays. Cell *185*, 1777-1792.e21. 10.1016/j.cell.2022.04.003.

bioRxiv preprint doi: https://doi.org/10.1101/2024.06.27.600930; this version posted July 2, 2024. The copyright holder for this preprint (which was not certified by peer review) is the author/funder, who has granted bioRxiv a license to display the preprint in perpetuity. It is made available under aCC-BY-NC-ND 4.0 International license.

36. Allen, W.E., Blosser, T.R., Sullivan, Z.A., Dulac, C., and Zhuang, X. (2023). Molecular and spatial signatures of mouse brain aging at single-cell resolution. Cell *186*, 194-208.e18. 10.1016/j.cell.2022.12.010.
37. Rodriques, S.G., Stickels, R.R., Goeva, A., Martin, C.A., Murray, E., Vanderburg, C.R., Welch, J., Chen, L.M., Chen, F., and Macosko, E.Z. (2019). Slide-seq: A Scalable Technology for Measuring Genome-Wide Expression at High Spatial Resolution. Science *363*, 1463–1467. 10.1126/science.aaw1219.
38. Ståhl, P.L., Salmén, F., Vickovic, S., Lundmark, A., Navarro, J.F., Magnusson, J., Giacomello, S., Asp, M., Westholm, J.O., Huss, M., et al. (2016). Visualization and analysis of gene expression in tissue sections by spatial transcriptomics. Science *353*, 78–82. 10.1126/science.aaf2403.
39. Miao, C., Cao, Q., Moser, M.-B., and Moser, E.I. (2017). Parvalbumin and Somatostatin Interneurons Control Different Space-Coding Networks in the Medial Entorhinal Cortex. Cell *171*, 507-521.e17. 10.1016/j.cell.2017.08.050.
40. Koenig, J., Linder, A.N., Leutgeb, J.K., and Leutgeb, S. (2011). The Spatial Periodicity of Grid Cells Is Not Sustained During Reduced Theta Oscillations. Science *332*, 592–595. 10.1126/science.1201685.
41. Brandon, M.P., Bogaard, A.R., Libby, C.P., Connerney, M.A., Gupta, K., and Hasselmo, M.E. (2011). Reduction of Theta Rhythm Dissociates Grid Cell Spatial Periodicity from Directional Tuning. Science *332*, 595–599. 10.1126/science.1201652.
42. Lian, B., Liu, M., Lan, Z., Sun, T., Meng, Z., Chang, Q., Liu, Z., Zhang, J., and Zhao, C. (2020). Hippocampal overexpression of SGK1 ameliorates spatial memory, rescues Aβ pathology and actin cytoskeleton polymerization in middle-aged APP/PS1 mice. Behavioural Brain Research *383*, 112503. 10.1016/j.bbr.2020.112503.
43. Ganfornina, M.D., Do Carmo, S., Martínez, E., Tolivia, J., Navarro, A., Rassart, E., and Sanchez, D. (2010). ApoD, a glia-derived apolipoprotein, is required for peripheral nerve functional integrity and a timely response to injury. Glia *58*, 1320–1334. 10.1002/glia.21010.
44. Hamilton, K.A., Wang, Y., Raefsky, S.M., Berkowitz, S., Spangler, R., Suire, C.N., Camandola, S., Lipsky, R.H., and Mattson, M.P. (2018). Mice lacking the transcriptional regulator Bhlhe40 have enhanced neuronal excitability and impaired synaptic plasticity in the hippocampus. PLoS One *13*, e0196223. 10.1371/journal.pone.0196223.
45. Stottmann, R.W., Driver, A., Gutierrez, A., Skelton, M.R., Muntifering, M., Stepien, C., Knudson, L., Kofron, M., Vorhees, C.V., and Williams, M.T. (2017). A heterozygous mutation in tubulin, beta 2B (Tubb2b) causes cognitive deficits and hippocampal disorganization. Genes Brain Behav *16*, 250–259. 10.1111/gbb.12327.
46. Wyeth, M.S., Pelkey, K.A., Petralia, R.S., Salter, M.W., McInnes, R.R., and McBain, C.J. (2014). Neto auxiliary protein interactions regulate kainate and NMDA receptor subunit localization at mossy fiber-CA3 pyramidal cell synapses. J Neurosci *34*, 622–628. 10.1523/JNEUROSCI.3098-13.2014.
47. Gall, D., Roussel, C., Susa, I., D'Angelo, E., Rossi, P., Bearzatto, B., Galas, M.C., Blum, D., Schurmans, S., and Schiffmann, S.N. (2003). Altered Neuronal Excitability in Cerebellar Granule Cells of Mice Lacking Calretinin. J. Neurosci. *23*, 9320–9327. 10.1523/JNEUROSCI.23-28-09320.2003.

bioRxiv preprint doi: https://doi.org/10.1101/2024.06.27.600930; this version posted July 2, 2024. The copyright holder for this preprint (which was not certified by peer review) is the author/funder, who has granted bioRxiv a license to display the preprint in perpetuity. It is made available under aCC-BY-NC-ND 4.0 International license.

48. Herz, J., Filiano, A.J., Wiltbank, A.T., Yogev, N., and Kipnis, J. (2017). Myeloid Cells in the Central Nervous System. Immunity *46*, 943–956. 10.1016/j.immuni.2017.06.007.
49. Kitamura, T., Pignatelli, M., Suh, J., Kohara, K., Yoshiki, A., Abe, K., and Tonegawa, S. (2014). Island Cells Control Temporal Association Memory. Science *343*, 896–901. 10.1126/science.1244634.
50. Sun, C., Kitamura, T., Yamamoto, J., Martin, J., Pignatelli, M., Kitch, L.J., Schnitzer, M.J., and Tonegawa, S. (2015). Distinct speed dependence of entorhinal island and ocean cells, including respective grid cells. Proc. Natl. Acad. Sci. U.S.A. *112*, 9466–9471. 10.1073/pnas.1511668112.
51. Suh, J., Rivest, A.J., Nakashiba, T., Tominaga, T., and Tonegawa, S. (2011). Entorhinal cortex layer III input to the hippocampus is crucial for temporal association memory. Science *334*, 1415–1420. 10.1126/science.1210125.
52. Hevner, R.F. (2007). Layer-Specific Markers as Probes for Neuron Type Identity in Human Neocortex and Malformations of Cortical Development: Journal of Neuropathology and Experimental Neurology *66*, 101–109. 10.1097/nen.0b013e3180301c06.
53. Franjic, D., Skarica, M., Ma, S., Arellano, J.I., Tebbenkamp, A.T.N., Choi, J., Xu, C., Li, Q., Morozov, Y.M., Andrijevic, D., et al. (2022). Transcriptomic taxonomy and neurogenic trajectories of adult human, macaque, and pig hippocampal and entorhinal cells. Neuron *110*, 452-469.e14. 10.1016/j.neuron.2021.10.036.
54. Zong, W., Wu, R., Li, M., Hu, Y., Li, Y., Li, J., Rong, H., Wu, H., Xu, Y., Lu, Y., et al. (2017). Fast high-resolution miniature two-photon microscopy for brain imaging in freely behaving mice. Nat Methods *14*, 713–719. 10.1038/nmeth.4305.
55. Apartis, E., Poindessous-Jazat, F., Epelbaum, J., and Bassant, M.H. (2000). Age-related changes in rhythmically bursting activity in the medial septum of rats. Brain Research *876*, 37–47. 10.1016/S0006-8993(00)02571-3.
56. Burjanadze, M.A., Dashniani, M.G., Solomonia, R.O., Beselia, G.V., Tsverava, L., Lagani, V., Chkhikvishvili, N.C., Naneishvili, T.L., Kruashvili, L.B., and Chighladze, M.R. (2022). Age-related changes in medial septal cholinergic and GABAergic projection neurons and hippocampal neurotransmitter receptors: relationship with memory impairment. Exp Brain Res *240*, 1589–1604. 10.1007/s00221-022-06354-2.
57. Barnes, C.A., Suster, M.S., Shen, J., and McNaughton, B.L. (1997). Multistability of cognitive maps in the hippocampus of old rats. Nature *388*, 272–275. 10.1038/40859.
58. Nakazono, T., Jun, H., Blurton-Jones, M., Green, K.N., and Igarashi, K.M. (2018). Gamma oscillations in the entorhinal-hippocampal circuit underlying memory and dementia. Neuroscience Research *129*, 40–46. 10.1016/j.neures.2018.02.002.
59. Muessig, L., Hauser, J., Wills, T.J., and Cacucci, F. (2015). A Developmental Switch in Place Cell Accuracy Coincides with Grid Cell Maturation. Neuron *86*, 1167–1173. 10.1016/j.neuron.2015.05.011.
60. Bjerknes, T.L., Moser, E.I., and Moser, M.-B. (2014). Representation of Geometric Borders in the Developing Rat. Neuron *82*, 71–78. 10.1016/j.neuron.2014.02.014.
61. Clark, B.J., and Taube, J.S. (2012). Vestibular and attractor network basis of the head direction cell signal in subcortical circuits. Front. Neural Circuits *6*. 10.3389/fncir.2012.00007.

bioRxiv preprint doi: https://doi.org/10.1101/2024.06.27.600930; this version posted July 2, 2024. The copyright holder for this preprint (which was not certified by peer review) is the author/funder, who has granted bioRxiv a license to display the preprint in perpetuity. It is made available under aCC-BY-NC-ND 4.0 International license.

62. McNaughton, B.L., Chen, L.L., and Markus, E.J. (1991). "Dead Reckoning," Landmark Learning, and the Sense of Direction: A Neurophysiological and Computational Hypothesis. Journal of Cognitive Neuroscience *3*, 190–202. 10.1162/jocn.1991.3.2.190.
63. Chen, G., Manson, D., Cacucci, F., and Wills, T.J. (2016). Absence of Visual Input Results in the Disruption of Grid Cell Firing in the Mouse. Current Biology *26*, 2335–2342. 10.1016/j.cub.2016.06.043.
64. Bishop, N.A., Lu, T., and Yankner, B.A. (2010). Neural mechanisms of ageing and cognitive decline. Nature *464*, 529–535. 10.1038/nature08983.
65. Barnes, C.A., and McNaughton, B.L. (1985). An age comparison of the rates of acquisition and forgetting of spatial information in relation to long-term enhancement of hippocampal synapses. Behav Neurosci *99*, 1040–1048. 10.1037//0735-7044.99.6.1040.
66. Burke, S.N., and Barnes, C.A. (2006). Neural plasticity in the ageing brain. Nat Rev Neurosci *7*, 30–40. 10.1038/nrn1809.
67. Harris, M.A., and Wolbers, T. (2012). Ageing effects on path integration and landmark navigation. Hippocampus *22*, 1770–1780. 10.1002/hipo.22011.
68. Bates, S.L., and Wolbers, T. (2014). How cognitive aging affects multisensory integration of navigational cues. Neurobiol Aging *35*, 2761–2769. 10.1016/j.neurobiolaging.2014.04.003.
69. Grubman, A., Chew, G., Ouyang, J.F., Sun, G., Choo, X.Y., McLean, C., Simmons, R.K., Buckberry, S., Vargas-Landin, D.B., Poppe, D., et al. (2019). A single-cell atlas of entorhinal cortex from individuals with Alzheimer's disease reveals cell-type-specific gene expression regulation. Nat Neurosci *22*, 2087–2097. 10.1038/s41593-019-0539-4.
70. Tang, Q., Ebbesen, C.L., Sanguinetti-Scheck, J.I., Preston-Ferrer, P., Gundlfinger, A., Winterer, J., Beed, P., Ray, S., Naumann, R., Schmitz, D., et al. (2015). Anatomical Organization and Spatiotemporal Firing Patterns of Layer 3 Neurons in the Rat Medial Entorhinal Cortex. J. Neurosci. *35*, 12346–12354. 10.1523/JNEUROSCI.0696-15.2015.
71. Steward, O., and Scoville, S.A. (1976). Cells of origin of entorhinal cortical afferents to the hippocampus and fascia dentata of the rat. J of Comparative Neurology *169*, 347–370. 10.1002/cne.901690306.
72. Canto, C.B., Wouterlood, F.G., and Witter, M.P. (2008). What Does the Anatomical Organization of the Entorhinal Cortex Tell Us? Neural Plasticity *2008*, 1–18. 10.1155/2008/381243.
73. Canto, C.B., Koganezawa, N., Beed, P., Moser, E.I., and Witter, M.P. (2012). All layers of medial entorhinal cortex receive presubicular and parasubicular inputs. J Neurosci *32*, 17620–17631. 10.1523/JNEUROSCI.3526-12.2012.
74. Schmidt-Hieber, C., and Häusser, M. (2013). Cellular mechanisms of spatial navigation in the medial entorhinal cortex. Nat Neurosci *16*, 325–331. 10.1038/nn.3340.
75. Schmidt-Hieber, C., and Häusser, M. (2014). How to build a grid cell. Phil. Trans. R. Soc. B *369*, 20120520. 10.1098/rstb.2012.0520.
76. Couey, J.J., Witoelar, A., Zhang, S.-J., Zheng, K., Ye, J., Dunn, B., Czajkowski, R., Moser, M.-B., Moser, E.I., Roudi, Y., et al. (2013). Recurrent inhibitory circuitry as a mechanism for grid formation. Nat Neurosci *16*, 318–324. 10.1038/nn.3310.

bioRxiv preprint doi: https://doi.org/10.1101/2024.06.27.600930; this version posted July 2, 2024. The copyright holder for this preprint (which was not certified by peer review) is the author/funder, who has granted bioRxiv a license to display the preprint in perpetuity. It is made available under aCC-BY-NC-ND 4.0 International license.

77. Zutshi, I., Fu, M.L., Lilascharoen, V., Leutgeb, J.K., Lim, B.K., and Leutgeb, S. (2018). Recurrent circuits within medial entorhinal cortex superficial layers support grid cell firing. Nat Commun *9*, 3701. 10.1038/s41467-018-06104-5.
78. Winterer, J., Maier, N., Wozny, C., Beed, P., Breustedt, J., Evangelista, R., Peng, Y., D'Albis, T., Kempter, R., and Schmitz, D. (2017). Excitatory Microcircuits within Superficial Layers of the Medial Entorhinal Cortex. Cell Reports *19*, 1110–1116. 10.1016/j.celrep.2017.04.041.
79. Moser, E.I., Moser, M.-B., and Roudi, Y. (2014). Network mechanisms of grid cells. Phil. Trans. R. Soc. B *369*, 20120511. 10.1098/rstb.2012.0511.
80. Schmidt, U., Weigert, M., Broaddus, C., and Myers, G. (2018). Cell Detection with Star-Convex Polygons. In Medical Image Computing and Computer Assisted Intervention – MICCAI 2018 Lecture Notes in Computer Science., A. F. Frangi, J. A. Schnabel, C. Davatzikos, C. Alberola-López, and G. Fichtinger, eds. (Springer International Publishing), pp. 265–273. 10.1007/978-3-030-00934-2_30.
81. Mathis, A., Mamidanna, P., Cury, K.M., Abe, T., Murthy, V.N., Mathis, M.W., and Bethge, M. (2018). DeepLabCut: markerless pose estimation of user-defined body parts with deep learning. Nat Neurosci *21*, 1281–1289. 10.1038/s41593-018-0209-y.
82. Fyhn, M., Molden, S., Witter, M.P., Moser, E.I., and Moser, M.-B. (2004). Spatial representation in the entorhinal cortex. Science *305*, 1258–1264. 10.1126/science.1099901.
83. Skaggs, W.E., McNaughton, B.L., Gothard, K.M., and Markus, E.J. (1993). An Information-Theoretic Approach to Deciphering the Hippocampal Code. Advances in Neural Information Processing Systems 5.
84. Fyhn, M., Hafting, T., Treves, A., Moser, M.-B., and Moser, E.I. (2007). Hippocampal remapping and grid realignment in entorhinal cortex. Nature *446*, 190–194. 10.1038/nature05601.
85. Langston, R.F., Ainge, J.A., Couey, J.J., Canto, C.B., Bjerknes, T.L., Witter, M.P., Moser, E.I., and Moser, M.-B. (2010). Development of the Spatial Representation System in the Rat. Science *328*, 1576–1580. 10.1126/science.1188210.
86. Giocomo, L.M., Stensola, T., Bonnevie, T., Van Cauter, T., Moser, M.-B., and Moser, E.I. (2014). Topography of Head Direction Cells in Medial Entorhinal Cortex. Current Biology *24*, 252–262. 10.1016/j.cub.2013.12.002.
87. Paxinos, G., and Keith B. J. Franklin, M. (2007). The Mouse Brain in Stereotaxic Coordinates (Elsevier Science).
88. Hao, Y., Hao, S., Andersen-Nissen, E., Mauck, W.M., Zheng, S., Butler, A., Lee, M.J., Wilk, A.J., Darby, C., Zager, M., et al. (2021). Integrated analysis of multimodal single-cell data. Cell *184*, 3573-3587.e29. 10.1016/j.cell.2021.04.048.
89. Korsunsky, I., Millard, N., Fan, J., Slowikowski, K., Zhang, F., Wei, K., Baglaenko, Y., Brenner, M., Loh, P., and Raychaudhuri, S. (2019). Fast, sensitive and accurate integration of single-cell data with Harmony. Nat Methods *16*, 1289–1296. 10.1038/s41592-019-0619-0.
90. Love, M.I., Huber, W., and Anders, S. (2014). Moderated estimation of fold change and dispersion for RNA-seq data with DESeq2. Genome Biol *15*, 550. 10.1186/s13059-014-0550-8.
91. Zhou, Y., Zhou, B., Pache, L., Chang, M., Khodabakhshi, A.H., Tanaseichuk, O., Benner, C., and Chanda, S.K. (2019). Metascape provides a biologist-oriented resource for the analysis of systems-level datasets. Nat Commun *10*, 1523. 10.1038/s41467-019-09234-6.

bioRxiv preprint doi: https://doi.org/10.1101/2024.06.27.600930; this version posted July 2, 2024. The copyright holder for this preprint (which was not certified by peer review) is the author/funder, who has granted bioRxiv a license to display the preprint in perpetuity. It is made available under aCC-BY-NC-ND 4.0 International license.

92. Yu, D., Huber, W., and Vitek, O. (2013). Shrinkage estimation of dispersion in Negative Binomial models for RNA-seq experiments with small sample size. Bioinformatics *29*, 1275–1282. 10.1093/bioinformatics/btt143.
93. Robinson, M.D., McCarthy, D.J., and Smyth, G.K. (2010). edgeR : a Bioconductor package for differential expression analysis of digital gene expression data. Bioinformatics *26*, 139–140. 10.1093/bioinformatics/btp616.
94. Miao, C., Cao, Q., Ito, H.T., Yamahachi, H., Witter, M.P., Moser, M.-B., and Moser, E.I. (2015). Hippocampal Remapping after Partial Inactivation of the Medial Entorhinal Cortex. Neuron *88*, 590–603. 10.1016/j.neuron.2015.09.051.
95. Boccara, C.N., Kjonigsen, L.J., Hammer, I.M., Bjaalie, J.G., Leergaard, T.B., and Witter, M.P. (2015). A three-plane architectonic atlas of the rat hippocampal region: 3D rat hippocampal atlas. Hippocampus *25*, 838–857. 10.1002/hipo.22407.
96. Bolger, A.M., Lohse, M., and Usadel, B. (2014). Trimmomatic: a flexible trimmer for Illumina sequence data. Bioinformatics *30*, 2114–2120. 10.1093/bioinformatics/btu170.
97. Dobin, A., Davis, C.A., Schlesinger, F., Drenkow, J., Zaleski, C., Jha, S., Batut, P., Chaisson, M., and Gingeras, T.R. (2013). STAR: ultrafast universal RNA-seq aligner. Bioinformatics *29*, 15–21. 10.1093/bioinformatics/bts635.
98. Pachitariu, M., Stringer, C., Dipoppa, M., Schröder, S., Rossi, L.F., Dalgleish, H., Carandini, M., and Harris, K.D. (2016). Suite2p: beyond 10,000 neurons with standard two-photon microscopy (Neuroscience) 10.1101/061507.
99. Friedrich, J., Zhou, P., and Paninski, L. (2017). Fast online deconvolution of calcium imaging data. PLoS Comput Biol *13*, e1005423. 10.1371/journal.pcbi.1005423.
100. Thevenaz, P., Ruttimann, U.E., and Unser, M. (1998). A pyramid approach to subpixel registration based on intensity. IEEE Trans. on Image Process. *7*, 27–41. 10.1109/83.650848.
101. Sheintuch, L., Rubin, A., Brande-Eilat, N., Geva, N., Sadeh, N., Pinchasof, O., and Ziv, Y. (2017). Tracking the Same Neurons across Multiple Days in Ca2+ Imaging Data. Cell Reports *21*, 1102–1115. 10.1016/j.celrep.2017.10.013.

Methods

Animals

JAX® C57BL/6J mice (The Jackson Laboratory, USA) were used in this study with the following characteristics: 21 young mice and 22 old mice, without gender bias, and with a weight of 22–35 g at implantation. 5 young and 10 old mice were used for tetrode recordings and for the 10x Genomics Visium analysis, 4 sections per mouse from the lateral to middle

bioRxiv preprint doi: https://doi.org/10.1101/2024.06.27.600930; this version posted July 2, 2024. The copyright holder for this preprint (which was not certified by peer review) is the author/funder, who has granted bioRxiv a license to display the preprint in perpetuity. It is made available under aCC-BY-NC-ND 4.0 International license.

part of the MEC were collected from 2 old (>28 months old), 2 young mice (<3 months old). For bulk RNA-seq analysis, 3 young and 3 old mice have been performed. For ISH, 4 young and 4 old mice were used. Visual discrimination learning task was done on 3 old and 4 young mice. Bglap3-Cre knock-in mice provided by Cyagen US Inc. by inserting P2A-Cre cassette downstream of Bglap3. In total, 37 Bglap3-Cre mice were used; among them, 3 mice were used for ISH and Cre expression verification, 7 mice were used for histology studies, 7 mice were used for *in vivo* calcium imaging studies and 20 mice were used for behavioral training. All mice were housed individually in transparent Plexiglass cages (35 cm × 30 cm × 30 cm) in a humidity- and temperature-controlled environment. All animals were maintained at 90% of free-feeding body weight on a 12-h light/12-h dark schedule. Testing occurred in the dark phase.

Bglap3-Cre mice were assessed by PCR using primer sequences below:

KI-F: 5'-CTCTTGTACAGTGTGGGAAGAGGAT-3',

KI-R: 5'-ATGTCCATCAGGTTCTTGCGA-3';

WT-F: 5'-GTTGTTCTGGGGTAGTCTCTATGACC-3',

WT-R: 5'-CTAAATTAACACAGGTACCAGGCG-3';

Surgery, virus injection, and electrode implantation

bioRxiv preprint doi: https://doi.org/10.1101/2024.06.27.600930; this version posted July 2, 2024. The copyright holder for this preprint (which was not certified by peer review) is the author/funder, who has granted bioRxiv a license to display the preprint in perpetuity. It is made available under aCC-BY-NC-ND 4.0 International license.

Before surgery, the animals were anesthetized with isoflurane (airflow: 0.8–1.0 L/min, 0.5–3% isoflurane, adjusted according to physiological condition). Isoflurane was gradually reduced from 3% to 1%. Depth of anesthesia was examined by testing tail and pinch reflexes as well as breathing. Subcutaneous injections of bupivacaine (Marcaine) and buprenorphine (Temgesic) were administered at the start of the surgery.

Upon induction of anesthesia, the animal was fixed in a Kopf stereotaxic frame for implantation of tetrodes. Holes were drilled in the skull above the right MEC. For virus injection in MEC, a 10 µL NanoFil syringe (World Precision Instruments, Sarasota, FL, USA) and a 33 gauge beveled metal needle were used to inject viruses in the MEC with the injection site: 0.3 mm anterior to the transverse sinus, 3.1–3.6 mm from the midline (ML axis), 1.8–1.5, 1.5–1.3 mm below the dura. For primary somatosensory barrel cortex (S1BF) virus injection, the injection site was 2.49 mm from the midline (ML axis), 1.0 mm posterior to Bregma and 0.35 mm below the dura. Injection volume (0.4–0.8 µL at each location) and flow rate (0.08 µL/min) were controlled with a Micro4™ Microsyringe Pump Controller (World Precision Instruments). After injection, the needle was left in place for 10 min before being slowly withdrawn.

For electrode implantation, each mouse was implanted with a VersaDrive-4 microdrive (NeuraLynx, Bozeman, MT, USA), connected to 4 tetrodes. The tetrodes were made of 17 µm polyimide-coated platinum-iridium (90%–10%) wire. The electrode tips were plated with

bioRxiv preprint doi: https://doi.org/10.1101/2024.06.27.600930; this version posted July 2, 2024. The copyright holder for this preprint (which was not certified by peer review) is the author/funder, who has granted bioRxiv a license to display the preprint in perpetuity. It is made available under aCC-BY-NC-ND 4.0 International license.

platinum to reduce electrode impedances to approximately 100–250 kΩ at 1 Hz. The tetrodes were inserted 0.35–0.40 mm anterior of the transverse sinus, 3.2–3.5 mm lateral to the midline in the right hemisphere, and 0.8–1.2 mm below the dura, at a 5° angle in the sagittal plane, with electrode tips pointing in the posterior direction. The microdrives were secured to the skull with jewelers' screws and dental cement. Two front screws were connected to ground.

Electrode turning and recording procedures

Turning of the tetrodes started 2–3 d after the surgery. Data collection began within 3 weeks. Testing of control animals was alternated with testing of experimental animals. Before each recording trial, the mouse rested on a towel in a large flowerpot on a pedestal. The mouse was connected to the recording equipment via AC-coupled unity-gain operational amplifiers close to the head and a counterbalanced cable that allowed the animal to move freely. Over the course of 20–60 d, the tetrodes were lowered in steps ≤50 μm until well-separated single neurons could be recorded. Data were collected when the signal amplitudes exceeded four times the noise level (20–30 μV) and single units were stable for more than 1 h.

Recorded signals were amplified 8000–25,000 times and band-pass filtered between 0.8 and 6.7 kHz. Triggered spikes were stored to disk at 48 kHz (50 samples per waveform, 8 bits/sample) with a 32-bit time stamp (clock rate at 96 kHz). Electroencephalograms (EEGs) were recorded single-ended from one of the electrodes. The local field potential was

bioRxiv preprint doi: https://doi.org/10.1101/2024.06.27.600930; this version posted July 2, 2024. The copyright holder for this preprint (which was not certified by peer review) is the author/funder, who has granted bioRxiv a license to display the preprint in perpetuity. It is made available under aCC-BY-NC-ND 4.0 International license.

amplified 3000–10,000 times, low-pass filtered at 500 Hz, sampled at 4800 Hz, and stored with the unit data. Through a video camera, the recording system obtained the position of two light-emitting diodes (LEDs) on the headstage of the mouse. The LEDs were tracked individually at a rate of 50 Hz. The two LEDs were separated by 4 cm and aligned with the body axis of the mice.

Over the course of 3–6 weeks following surgery, the mice were first trained to run in a 1 m square black aluminum enclosure polarized by a cue card with white and black stripes. In mice with putative border cells, these trials were occasionally succeeded by a test in the same box with a 50 cm long and 50 cm high wall insert in the center of the box (Figure S3B). Each trial was 15 min. Running was motivated by scattering crumbs of chocolate at random locations in the box at 10–15 s intervals.

Histological procedures and electrode positions

The mice received an overdose of pentobarbital and were subsequently perfused intracardially with saline followed by either 4% formaldehyde or 4% freshly depolymerized paraformaldehyde (PFA) in phosphate buffer. The brains were extracted and stored in the same fixative, and frozen sagittal sections (10 µm) were cut on a cryostat. Every 10^{th} section was stained with cresyl violet. All sections of the infected and implanted part of the MEC were collected. Tetrodes were identified and the tip of each electrode was found by comparison with adjacent sections.

bioRxiv preprint doi: https://doi.org/10.1101/2024.06.27.600930; this version posted July 2, 2024. The copyright holder for this preprint (which was not certified by peer review) is the author/funder, who has granted bioRxiv a license to display the preprint in perpetuity. It is made available under aCC-BY-NC-ND 4.0 International license.

Tissue preparation for 10x Genomics Visium technology

The 10x Genomics Visium experiment was performed according to the company's protocol (https://www.10xgenomics.com/platforms/visium) with the simplified streamline of experiments shown in Figure 3A. Fresh frozen brain tissues were embedded, sectioned, and placed onto the Capture Area of the gene expression slide. Each Capture Area has thousands of barcoded spots containing millions of capture oligonucleotides with spatial barcodes unique to that spot. We utilized standard H&E fixation and staining techniques using a brightfield microscope to visualize tissue sections on slides. The tissue was permeabilized to release mRNA from the cells, which bound to the spatially barcoded oligonucleotides present on the spots. Reverse transcription was then performed to produce cDNA from the captured mRNA. The barcoded cDNA was then pooled for downstream processing to generate a sequencing-ready library. For formalin-fixed paraffin-embedded (FFPE) tissues, the tissue was permeabilized to release ligated probe pairs from the cells, which bound to the spatially barcoded oligonucleotides present on the spots. Spatial barcodes were added via an extension reaction. The barcoded molecules were then pooled for downstream processing to generate a sequencing-ready library. The resulting 10× barcoded library was processed with standard NGS short-read sequencing on Illumina sequencers for massive transcriptional profiling of entire tissue sections.

Bulk RNA sequencing sample extraction and library preparation

bioRxiv preprint doi: https://doi.org/10.1101/2024.06.27.600930; this version posted July 2, 2024. The copyright holder for this preprint (which was not certified by peer review) is the author/funder, who has granted bioRxiv a license to display the preprint in perpetuity. It is made available under aCC-BY-NC-ND 4.0 International license.

Brain tissues were extracted from mice that were anesthetized with isoflurane gas. Next, MEC tissue was isolated and homogenized in TRIzol, followed by phase separation with chloroform. RNA was precipitated using isopropanol, washed with ethanol, and air-dried before resuspension in DEPC-treated water. The quality and concentration of RNA were measured. All samples with RNA Integrity Number (RIN) > 8 were used as input to library construction.

RT-qPCR

The procedure was the same as mentioned above. The quality and concentration of RNA were measured, followed by cDNA synthesis. qPCR was performed using SYBR Green to quantify target gene expression levels, with *GAPDH* as the reference gene.

Primer sequences: *Bglap3* (F): CTGACAAAGCCTTCATGTCC, (R): TCAAGCTCACATAGCTCCC; *GAPDH* (F): AGGTCGGTGTGAACGGATTTG, (R): TGTAGACCATGTAGTTGAGGTCA.

RNAscope in situ hybridization

Brain tissues were collected from mice anesthetized with isoflurane gas. The tissue was then placed in a container embedded with optical cutting temperature (OCT) Compound (4583, Sakura, Tokyo, Japan), placed on dry ice for freezing, and transferred to a cryostat pre-cooled to -20 °C for 1 h. Once the tissue temperature equilibrated, brain slices of 20 μm thickness were cut in a cryostat chamber with temperature adjusted to -10 °C following

bioRxiv preprint doi: https://doi.org/10.1101/2024.06.27.600930; this version posted July 2, 2024. The copyright holder for this preprint (which was not certified by peer review) is the author/funder, who has granted bioRxiv a license to display the preprint in perpetuity. It is made available under aCC-BY-NC-ND 4.0 International license.

standard cryosectioning procedures, and mounted onto glass slides. The slides were placed at -20 °C for 20 min and then subjected to the following steps: fixation in 10% neutral formalin solution at 4 °C, dehydration, hydrophobic circle drawing, and treatment with hydrogen peroxide and proteinase IV. The slices were then processed using RNAscope® Multiplex Fluorescent Reagent Kit V2 (323100, Advanced Cell Diagnostics, Inc., Newark, CA, USA). according to manufacturer's instructions, which includes probe hybridization; AMP1, AMP2, and AMP3 incubation; and Opal 570 and Opal 520 fluorescence labeling. Finally, the slices were then DAPI-stained. A cover slip with a mounting medium containing anti-fading agent was placed on top, and the slides were immediately examined or stored at 4 °C. Subsequent confocal imaging was conducted on the Nikon A1R confocal microscope with a 60× oil immersion objective lens. Image analysis was performed using HALO software (Indica Labs Inc., Albuquerque, NM, USA).

Axonal labeling and retrograde viral tracing

For axonal labeling, 0.4 μL of AAV2/9-hSyn-DIO-Synaptophysin-EGFP (2.98×10^{12} VG/mL; BrainVTA (Wuhan) Co., Ltd., Wuhan, China) was injected in the MEC (ML: +3.1~3.6; AP: sinus + 0.3; DV: -1.8~1.5, -1.5~1.3) with a Nanoliter 2010 Microinjection Pump (World Precision Instruments). For rabies tracing, 0.4 μL mixture of AAV2/8-DIO-EGFP-TVA and AAV2/8-DIO-oRVG (2.73×10^{12} VG/mL and 5.10×10^{12} ;BrainVTA (Wuhan) Co., Ltd., Wuhan) was injected in the MEC as the same location mentioned above. After three weeks,

bioRxiv preprint doi: https://doi.org/10.1101/2024.06.27.600930; this version posted July 2, 2024. The copyright holder for this preprint (which was not certified by peer review) is the author/funder, who has granted bioRxiv a license to display the preprint in perpetuity. It is made available under aCC-BY-NC-ND 4.0 International license.

0.8 μL of rabies virus EnvA-RVdG-mCherry (gift from Weixiang Guo Lab) was injected at the same location. Brain was collected one week after rabies virus injection.

Perfusion, cryosectioning, and fluorescence slice preparation

Mice were administered a 0.5 mL intraperitoneal injection of 2.5% tribromoethanol and securely fixed on an operating table once they showed no pain reflexes. The abdominal cavity was opened from below the sternum, and the chest was exposed by cutting the diaphragm. The right atrium was excised with scissors, followed by the insertion of a perfusion needle into the left ventricle. A total of 20 mL of physiological saline was perfused using a perfusion pump at a rate of 5 mL/min until the liver lost its natural color. Subsequently, 20 mL of 4% PFA was perfused at the same flow rate. The mouse's head was then severed from the neck, the skull was carefully dissected using fine forceps, and the brain tissue was removed and immersed in PFA for 24 h for fixation. The brain tissue was subsequently dehydrated in a 30% sucrose solution and left to soak for >24 h until the brain settled to the bottom.

Brain tissue sections were prepared using a cryostat microtome. The fixed and dehydrated mouse brain was carefully removed from the surface sucrose solution and excess liquid was blotted. The brain was then secured onto a metal mounting platform embedded with OCT Compound (4583, Sakura, Tokyo, Japan). A layer of OCT was applied to the surface of the brain tissue, and the prepared tissue was placed in the cryostat for freezing. The

bioRxiv preprint doi: https://doi.org/10.1101/2024.06.27.600930; this version posted July 2, 2024. The copyright holder for this preprint (which was not certified by peer review) is the author/funder, who has granted bioRxiv a license to display the preprint in perpetuity. It is made available under aCC-BY-NC-ND 4.0 International license.

frozen tissue was then sectioned at a thickness of 30 μm. Using a fine brush, the desired brain sections were flattened on the sample stage. A glass slide was brought close to the brain sections, and the temperature differential was used to adhere the brain sections onto the glass slide. The cryostat chamber temperature, as well as the temperatures of the blade and sample stage, were maintained at - 20 °C throughout the sectioning process.

Brain sections with fluorescence were dried under open air, rinsed with PBST (0.3% Triton-X100) for 10 min, stained with DAPI (1:1000) for 10 min, and sealed with a sealing medium. For immunofluorescence staining, brain slices were incubated in blocking solution (10% normal goat serum PBST, 1% Triton-X100) freely floating for two hours at room temperature, followed by incubation with primary antibodies NeuN (ab190565; 1:500) and GAD67 (ab75712; 1:100) in the blocking solution for three nights at 4 °C. After washing in PBST 10 mins for three times, the secondary antibody (A11039, Invitrogen; 1:500) was added and incubated for 2 hours at room temperature. Then, by washing for another 10 mins for three times, the brain tissues were mounted on the slices and the slices were sealed with a sealing medium. Imaging was processed using a Nikon A1R confocal microscope with a 20× objective lens. Fluorescence cells were counted manually.

c-Fos staining and image processing

c-Fos immunostaining was performed under the same procedure mentioned previously. Primary antibody c-Fos (226008, Synaptic System; 1:1000) was incubated at 4 °C for one

bioRxiv preprint doi: https://doi.org/10.1101/2024.06.27.600930; this version posted July 2, 2024. The copyright holder for this preprint (which was not certified by peer review) is the author/funder, who has granted bioRxiv a license to display the preprint in perpetuity. It is made available under aCC-BY-NC-ND 4.0 International license.

night, followed by secondary antibody (A11034, Invitrogen; 1:500) incubation for one hour at room temperature.

c-Fos+ cells were identified with ImageJ/Fiji plugin StarDist [80] using the Versatile (fluorescent nuclei) model. c-Fos+ cell whose Feret's Diameter was between 8 to 16 μm was selected and the fluorescence intensity of individual c-Fos+ cells was measured by their Mean Gray Value in arbitrary units. Bglap3 positive or negative cells were identified whether the Mean Gray Value of mCherry signals was higher or lower than 1000.

Water maze behavioral training

The water maze had a diameter of 120 cm. In the training phase, distinctive visual cues of different shapes and colors were placed along the inner walls in the east, west, south, and north directions. A 15 cm diameter underwater escape platform was located in the southeast direction, 25 cm away from the maze's edge. The maze perimeter was surrounded by light-blocking curtains. Mice received intraperitoneal injections (i.p.) of either Deschloroclozapine (DCZ) (MedChemexpress, HY-42110) (0.1 mg/kg) or saline 30 min before behavioral training. During the training phase, mice were placed into the water facing the maze walls, with the starting position randomly selected from one of the four directions: east, west, south, or north. The time taken by the animal to locate the escape platform was recorded. If the time exceeded 90 s, the animal was guided to the platform and allowed to stay there for 10 s. Each mouse underwent four training trials per day, starting from different directions (east,

bioRxiv preprint doi: https://doi.org/10.1101/2024.06.27.600930; this version posted July 2, 2024. The copyright holder for this preprint (which was not certified by peer review) is the author/funder, who has granted bioRxiv a license to display the preprint in perpetuity. It is made available under aCC-BY-NC-ND 4.0 International license.

west, south, or north) each time. The mice were dried in a drying chamber and returned to their cages after each training session. The inter-trial interval was 15–20 min, and the training continued for 5–6 d. For the 'New location' session, the platform was placed on the opposite quadrant and the mice learned the new location of the platform for five days. For the 'Dark' session, LED light was replaced with infrared light and the cues were removed. To measure path-integration maze learning, the mice needed to find the platform using the start box as a reference.

The trajectories of the animals were labeled using DeepLabCut, a deep neural network-based tracking method [81]. Information such as the water maze area, escape platform location, and start and end frames for each trial were manually assigned. Time taken by the mice to find the platform, distance traveled, and swimming speed and trajectory heatmaps were calculated using MATLAB code developed by the lab.

Visual discrimination learning task

The task was done in an operation box that is 40*35*40 cm, with a touch screen placed at one of the interior walls. In the pre-learning stage, a random image appears randomly on the touch screen every 25 seconds. Once the mice touches the image, it will be rewarded with chocolate beans in the opposite food trough. This encouraged the mice to actively touch the image establishing an association between touching the picture and receiving a reward. A chocolate reward for a mouse is counted as one trial. Each mouse does 30 trials

bioRxiv preprint doi: https://doi.org/10.1101/2024.06.27.600930; this version posted July 2, 2024. The copyright holder for this preprint (which was not certified by peer review) is the author/funder, who has granted bioRxiv a license to display the preprint in perpetuity. It is made available under aCC-BY-NC-ND 4.0 International license.

or 30 minutes per day. In the learning stage, two distinct images appear on the touch screen at the same time. By touching the correct one the mouse receives a chocolate reward, otherwise, by touching the wrong picture the mouse receives a short light penalty. Each mouse performs 30 trials or 60 minutes every day, and the test is continued for 1 to 2 months with each period of 10 days considered as one learning stage. The success of each mouse was assessed on a daily basis, and the accuracy rate was calculated. If a mouse achieved an accuracy rate exceeding 70% for three consecutive days, it was deemed to have successfully learned the task.

Prism implantation and Miniaturized 2-photon microscope calcium imaging

A 0.4 μL mixture of AAV2/9-CaMKIIa-DIO-hM4D(Gi)-mCherry-WPRE-hGH with AAV2/9-hSyn-GCaMP6s-WPRE-hGH (5.01 × 10^{12} VG/mL, 5.27 × 10^{12} VG/mL; BrainVTA (Wuhan) Co., Ltd., Wuhan, China) was injected in the MEC (ML: +3.1~3.6; AP: sinus + 0.3; DV: -1.8~1.5, -1.5~1.3) with a Nanoliter 2010 Microinjection Pump (World Precision Instruments). Three weeks after injection, mice were anesthetized with isoflurane, and a small square cranial window (2.5 × 2.5 mm^2) was made and centered over the targeted cortex. The dura was carefully removed, and a small glass prism (3.5 × 2.5 mm^2) was placed along the dorsoventral surface of the MEC between the cerebrum and cerebellum. After recovery for one week, the headstage was mounted to the skull of each mouse. To increase the imaging stability, 1.5% low-melting-point agarose was added to the objective of the brain tissue. After adaptation, we restrained each mouse with a body holder and used the benchtop TPM

bioRxiv preprint doi: https://doi.org/10.1101/2024.06.27.600930; this version posted July 2, 2024. The copyright holder for this preprint (which was not certified by peer review) is the author/funder, who has granted bioRxiv a license to display the preprint in perpetuity. It is made available under aCC-BY-NC-ND 4.0 International license.

to confirm the region of viral infection (ROI). We then mounted the fast, high-resolution, miniaturized TPM (FHIRM-TPM) to the ROI designated by the benchtop TPM. Next, we glued a headstage to the skull during craniotomy preparation and protected the attachment with dental cement. During imaging trials, the mice were trained in a 1 m square black aluminum enclosure polarized by a white cue card, and the calcium signals were collected with the miniaturized TPM, according to previously published methods[54]. Each trial was 40 min. Running was motivated by scattering crumbs of cookies at random locations in the box at 10–15 s intervals. Mice received Deschloroclozapine (DCZ) injection in the same way described above.

Statistical analysis

Rate maps, firing fields, and spatial information

Position estimates were based on tracking of LEDs on the headstage connected to the microdrive. Tracked positions were smoothed with a 15 point mean filter offline. To characterize firing fields, the position data were sorted into bins of 3 × 3 cm^2 and the firing rate was determined for each bin. A spatial smoothing algorithm was used [82]. The average rate in any bin *x* was estimated as:

$$\lambda(x) = \sum_{i=1}^{n} g(\frac{s_i - x}{h}) \Big/ \int_0^T g(\frac{y(t) - x}{h}) dt$$

bioRxiv preprint doi: https://doi.org/10.1101/2024.06.27.600930; this version posted July 2, 2024. The copyright holder for this preprint (which was not certified by peer review) is the author/funder, who has granted bioRxiv a license to display the preprint in perpetuity. It is made available under aCC-BY-NC-ND 4.0 International license.

Where *g* is a smoothing kernel, *h* is a smoothing factor, *n* is the number of spikes, s_i the location of the *i*-th spike, *y(t)* is the location of the mice at time *t*, and [*0*, *T*] is the recording period. A Gaussian kernel was used with *g* and *h* = 3. In order to avoid error from extrapolation, we considered positions more than 3 cm away from the tracked path as unvisited.

The cell's peak rate was estimated as the highest firing rate observed in any bin of the smoothed rate map. For each cell, the spatial information content in bits per spike [83]was calculated as:

$$\text{information content} = \sum p_i \frac{\lambda_i}{\lambda} \log_2 \frac{\lambda_i}{\lambda}$$

where λ_i is the mean firing rate of a unit in the *i*-th bin, λ is the overall mean firing rate, and p_i is the probability of the animal being in the *i*-th bin (occupancy in the *i*-th bin / total recording time).

Analysis of grid cells

Our methods for grid cell analysis were adapted from those described in previous studies [84,85]. For all cells with more than 100 spikes, we calculated the spatial autocorrelation for each smoothed rate map. Autocorrelograms were based on Pearson's product moment correlation coefficient with corrections for edge effects and unvisited locations. With $\lambda(x, y)$ denoting the average rate of a cell at location *(x, y)*, the autocorrelation between the fields with spatial lags of τ_x and τ_y was estimated as:

bioRxiv preprint doi: https://doi.org/10.1101/2024.06.27.600930; this version posted July 2, 2024. The copyright holder for this preprint (which was not certified by peer review) is the author/funder, who has granted bioRxiv a license to display the preprint in perpetuity. It is made available under aCC-BY-NC-ND 4.0 International license.

$$r(\tau_x, \tau_y) = \frac{n\sum \lambda(x,y)\lambda(x-\tau_x, y-\tau_y) - \sum \lambda(x,y) \sum \lambda(x-\tau_x, y-\tau_y)}{\sqrt{n\sum \lambda(x,y)^2 - (\sum \lambda(x,y))^2}\sqrt{n\sum \lambda(x-\tau_x, y-\tau_y)^2 - (\Sigma \lambda(x-\tau_x, y-\tau_y))^2}}$$

where the summation is over all n pixels in $\lambda(x, y)$ for which the rate was estimated for both $\lambda(x, y)$ and $\lambda(x - \tau_x, y - \tau_y)$. Autocorrelations were not estimated for lags of τ_x, τ_y where $n < 20$.

The degree of spatial periodicity ('grid score') was determined for each recorded cell by taking a circular sample of the autocorrelogram, centered on but excluding the central peak, and comparing rotated versions of this sample. The Pearson correlation of this circle with its rotation in α degrees was obtained for angles of 60° and 120° on one side and 30°, 90°, and 150° on the other. The cell's grid score was defined as the minimum difference between any of the elements in the first group and any of the elements in the second. Shuffling was performed for each cell individually with 1000 permutations for each cell. In each permutation, the entire sequence of the spikes or the cell's deconvolved calcium activity was time-shifted along the animal's path by a random interval between 30 s on one side and 30 s on the other side less than the length of the session, with the end of the session wrapped to the beginning. The grid score of each data shuffle was calculated according to previously described methods [85]. If the grid score from the recorded data was larger than the 99th percentile of grid scores in the distribution from the 1000 permutations of shuffled data of the same cell, the cell was defined as a grid cell. In calcium imaging analysis, stable

bioRxiv preprint doi: https://doi.org/10.1101/2024.06.27.600930; this version posted July 2, 2024. The copyright holder for this preprint (which was not certified by peer review) is the author/funder, who has granted bioRxiv a license to display the preprint in perpetuity. It is made available under aCC-BY-NC-ND 4.0 International license.

grid cells were defined as those with a spatial correlation greater than 0.3 between the two baseline sessions, and a grid score exceeding the 95th percentile of the shuffle distribution in at least one baseline session.

Analysis of head direction cells

Our methods for analyzing head direction cells have been reported in previous studies [85,86]. The mouse's head direction was calculated for each tracker sample from the projection of the relative position of the two LEDs onto the horizontal plane. The directional-tuning function for each cell was obtained by plotting firing rate as a function of the mouse's directional heading, divided into bins of 3° and smoothed with a 30° mean window filter (five bins on each side). The preferred firing direction was defined by the mean vector of the directional-tuning function.

Head direction-modulated cells were defined as cells with mean vector lengths significantly exceeding the degree of directional tuning that would be expected by chance. Chance values were determined by a shuffling procedure performed in the same way as for grid cells and using a similar number of permutations per cell. Cells were defined as a head direction cell (HD) if the mean vector from the recorded data was larger than the 99th percentile of the mean vector in the distribution from the 1000 permutations of shuffled data of the same cell. In calcium imaging analysis, stable head direction cells were defined as those with an HD tuning correlation greater than 0.3 between the two baseline sessions, a

bioRxiv preprint doi: https://doi.org/10.1101/2024.06.27.600930; this version posted July 2, 2024. The copyright holder for this preprint (which was not certified by peer review) is the author/funder, who has granted bioRxiv a license to display the preprint in perpetuity. It is made available under aCC-BY-NC-ND 4.0 International license.

difference in preferred angles of no more than 30 degrees, and a mean vector length exceeding the 95th percentile of the shuffle distribution in at least one baseline session, while not having a grid score surpassing that of the shuffle distribution.

Analysis of border cells

Our methods for analyzing border cells are based on previous reports [18,60]. Border cells were identified by the score resulting from the following computation: For each cell with an average rate above 0.2 Hz, the border score was the difference between the maximal length of a wall touching on any single firing field of the cell and the average distance of the field from the nearest wall, divided by the sum of those values. Border scores thus ranged from -1 for cells with infinitely small central fields to +1 for cells with infinitely narrow fields that lined up perfectly along the entire wall.

Border cells were defined as cells with border scores significantly exceeding chance levels determined by a shuffling procedure performed in the same way as for grid cells, using a similar number of permutations per cell, but with the addition of a spatial information criterion [60]. Cells were defined as border cells if two conditions were met: (i) The border score from the recorded data was larger than the 99th percentile of border scores in the distribution from the 1000 permutations of shuffled data of the same cell, and (ii) the spatial information content in the recorded data was higher than the 99th percentile value for spatial information in the shuffled data. In calcium imaging analysis, stable border cells were defined as those

bioRxiv preprint doi: https://doi.org/10.1101/2024.06.27.600930; this version posted July 2, 2024. The copyright holder for this preprint (which was not certified by peer review) is the author/funder, who has granted bioRxiv a license to display the preprint in perpetuity. It is made available under aCC-BY-NC-ND 4.0 International license.

with a spatial correlation greater than 0.3 between the two baseline sessions, and a border score exceeding the 95th percentile of the shuffle distribution in at least one baseline session. Spatial cells were defined as those with a spatial correlation greater than 0.3 between the two baseline sessions, and spatial information content in both baseline sessions exceeding the 95th percentile of the shuffle distribution, excluding grid, border and head direction cells.

Analysis of speed cells

Our methods for analyzing speed cells are similar to those reported in a previous study [19]. The instantaneous firing rate was obtained by dividing the whole trial into 20 ms bins, coinciding with the frames of the tracking camera. A temporal histogram of spiking was then smoothed with a 250 ms-wide Gaussian filter. The speed score for each cell was defined as the Pearson product-moment correlation between the cell's instantaneous firing rate and the mouse's instantaneous running speed, on a scale from -1 to 1. A cell was defined as a speed cell if the speed score from the recorded data was larger than the 99th percentile of speed scores in the distribution from the 1000 permutations of shuffled data of the same cell. Shuffling was performed in the same way as for grid cells and head direction cells.

LFP power spectrum analysis

The power spectrum was computed through a parametric spectral estimation technique, termed the Modified Covariance Method. This approach incorporates an Auto-Regressive

bioRxiv preprint doi: https://doi.org/10.1101/2024.06.27.600930; this version posted July 2, 2024. The copyright holder for this preprint (which was not certified by peer review) is the author/funder, who has granted bioRxiv a license to display the preprint in perpetuity. It is made available under aCC-BY-NC-ND 4.0 International license.

(AR) model, preset with an order of 30, to forecast the spectrum by leveraging the Fourier Transform of the EEG data. The spectral density estimation spans a frequency range from 0 to 31.3 Hz. This range facilitates a precise quantification of power distribution throughout the EEG signal's frequency spectrum. Following this, we determined the mean power for both young and aged mice, specifically within the theta (6 -12Hz) and low gamma (20 - 30Hz) frequency bands.

10x Genomics Visium data analysis

Raw Illumina sequencing data was processed with Space Ranger (v2.1) for sample demultiplexing, image alignment, barcode processing, and gene counting. The output file could be displayed Loupe Browser (v7) software to visualize gene expression patterns across brain slices. MEC and its subregions were assigned based on Franklin's *The Mouse Brain in Stereotaxic Coordinates, Third Edition* [87] and the spatial barcodes were extracted for further analysis. Feature-barcode matrices from different mice were merged in R using Seurat package [88] following Harmony for batch correction [89], and UMAP visualization of dimensional reduction and cluster displaying. After extracting the data based on barcodes from entire MEC or sublayers of MEC, normalization and differential expression of MEC or sublayers between old and young mice was done with DEseq2 in R [90], with a threshold that was set to absolute Log_2 Fold-Change > 0.5, adjusted P-value < 0.05. Enrichment network analysis of differentially expressed genes was done with Metascape. [91] Differential expressions of genes

bioRxiv preprint doi: https://doi.org/10.1101/2024.06.27.600930; this version posted July 2, 2024. The copyright holder for this preprint (which was not certified by peer review) is the author/funder, who has granted bioRxiv a license to display the preprint in perpetuity. It is made available under aCC-BY-NC-ND 4.0 International license.

presented in Figure S8 were calculated in Loupe Browser 7 using algorithms sSeq [92]and edgeR [93].

10x Genomics Visium image analysis

Boundaries of the MEC with neighboring regions, such as the postrhinal cortex, parasubiculum, presubiculum, lateral entorhinal cortex, and subiculum, were defined as previously described [94]. Unfolded MEC maps were prepared for each sagittal brain section by mapping the dorsal border of the MEC onto a straight line. For each section, the surface length of the MEC was measured using Image-Pro Plus software (Media Cybernetics, Rockville, MD, USA) and subsequently mapped onto a straight line perpendicular to the line that represents the dorsal border. All borders were established using cytoarchitectonic criteria that can reliably be established irrespective of the plane of sectioning, as described in detail for the rat brain [95]. These borders, as defined in the rat, can be reliably applied to the mouse brain [94].

Bulk RNA sequencing data analysis

RNA raw data was first analyzed by Fastqc (http://www.bioinformatics.babraham.ac.uk/projects/fastqc) for quality control, then we used Trimmomatic (v0.39) [96] to filter low-quality reads and trim the linker sequence. Reads were aligned to the GRCm39 reference genome using STAR (2.7.5c) [97]. After comparing with the reference genome, featureCounts was conducted for gene quantification to get the

bioRxiv preprint doi: https://doi.org/10.1101/2024.06.27.600930; this version posted July 2, 2024. The copyright holder for this preprint (which was not certified by peer review) is the author/funder, who has granted bioRxiv a license to display the preprint in perpetuity. It is made available under aCC-BY-NC-ND 4.0 International license.

raw counts matrix for downstream analysis. The differential expression analysis was done by DESeq2 [90] in R setting the threshold as: absolute Log2 Fold-Change > 0.5, adjusted P-value < 0.05.

Calcium imaging data analysis

Calcium imaging data were preprocessed using Suite2p [98](https://github.com/MouseLand/suite2p), a popular open-source pipeline for calcium imaging data analysis. This involved motion correction to counteract minor drifts in the imaging plane over the session, automated region of interest (ROI) extraction to identify individual neuronal cells based on their spatial footprints and temporal activity patterns, and extracting fluorescence signals (F_{raw}) from the ROIs. We manually curated and removed ROIs with poor morphological characteristics or subpar fluorescence signals. Custom MATLAB (R2020b) scripts were used for further analysis. For each detected neuron, the baseline fluorescence (F_0) was gauged from the lower 8th percentile of the trace, with the ΔF/F signal calculated as $(F_{raw} - F_0)/F_0$ correspondingly. The ΔF/F signal underwent wavelet denoising using the 'wdenoise' function to eliminate noise while preserving salient features of the signal. Subsequently, we employed the OASIS [99](https://github.com/zhoupc/OASIS_matlab) algorithm for deconvolution to infer the underlying spiking activity from the denoised ΔF/F signal. To further refine our detection of significant calcium events, we defined a time window in the ΔF/F signal as a 'significant term' if its amplitude exceeded twice the local standard deviation. Only the deconvolved

bioRxiv preprint doi: https://doi.org/10.1101/2024.06.27.600930; this version posted July 2, 2024. The copyright holder for this preprint (which was not certified by peer review) is the author/funder, who has granted bioRxiv a license to display the preprint in perpetuity. It is made available under aCC-BY-NC-ND 4.0 International license.

calcium events falling within this designated significant term were retained for subsequent analyses. Neuronal activity was correlated with the animal's position and movement in the arena to identify spatially-modulated cells.

Cell cross-session alignment and Bglap3 +/- cells classification

To effectively distinguish between Bglap3 positive and Bglap3-negative neurons in MEC, we employed custom MATLAB scripts to align the scanned red channel field of view with the green channel field of view. In image processing, 2D cross-correlation serves as a robust method to compute similarity between two images. We computed cross-correlations between maximum intensity projection images outputted by Suite2p from different channels and sessions. The xy displacements corresponding to the maximum cross-correlation between two fields of view were employed as translation offsets for alignment corrections. If further alignment was required, the translationally-aligned image stacks were subjected to secondary alignment using MultiStackReg [100]. MultiStackReg is an open-source ImageJ batch alignment plugin developed on top of Turboreg, which offers five versatile transformation registration modalities and is widely applied in image registration. From this process, we obtained the transformation matrices. Each session's cellular footprints were then subjected to transformations. Using the transformed and aligned cell footprints as input to CellReg [101](https://github.com/zivlab/CellReg), a previously published neuron cross-day alignment tool, we identified cells that consistently appeared across imaging days. These

bioRxiv preprint doi: https://doi.org/10.1101/2024.06.27.600930; this version posted July 2, 2024. The copyright holder for this preprint (which was not certified by peer review) is the author/funder, who has granted bioRxiv a license to display the preprint in perpetuity. It is made available under aCC-BY-NC-ND 4.0 International license.

cells were then classified into Bglap3 positive or Bglap3 negative categories based on their presence in the red channel.

Approvals

Experiments were performed according to the Animal Welfare/Ethics guidelines in Peking University, the Norwegian Animal Welfare Act, and the European Convention for the Protection of Vertebrate Animals used for Experimental and Other Scientific Purposes. The experiments were approved by the National Animal Research Authorities of Norway and the Animal Research Authorities of Peking University.

bioRxiv preprint doi: https://doi.org/10.1101/2024.06.27.600930; this version posted July 2, 2024. The copyright holder for this preprint (which was not certified by peer review) is the author/funder, who has granted bioRxiv a license to display the preprint in perpetuity. It is made available under aCC-BY-NC-ND 4.0 International license.

bioRxiv preprint doi: https://doi.org/10.1101/2024.06.27.600930; this version posted July 2, 2024. The copyright holder for this preprint (which was not certified by peer review) is the author/funder, who has granted bioRxiv a license to display the preprint in perpetuity. It is made available under aCC-BY-NC-ND 4.0 International license.

Main Figures

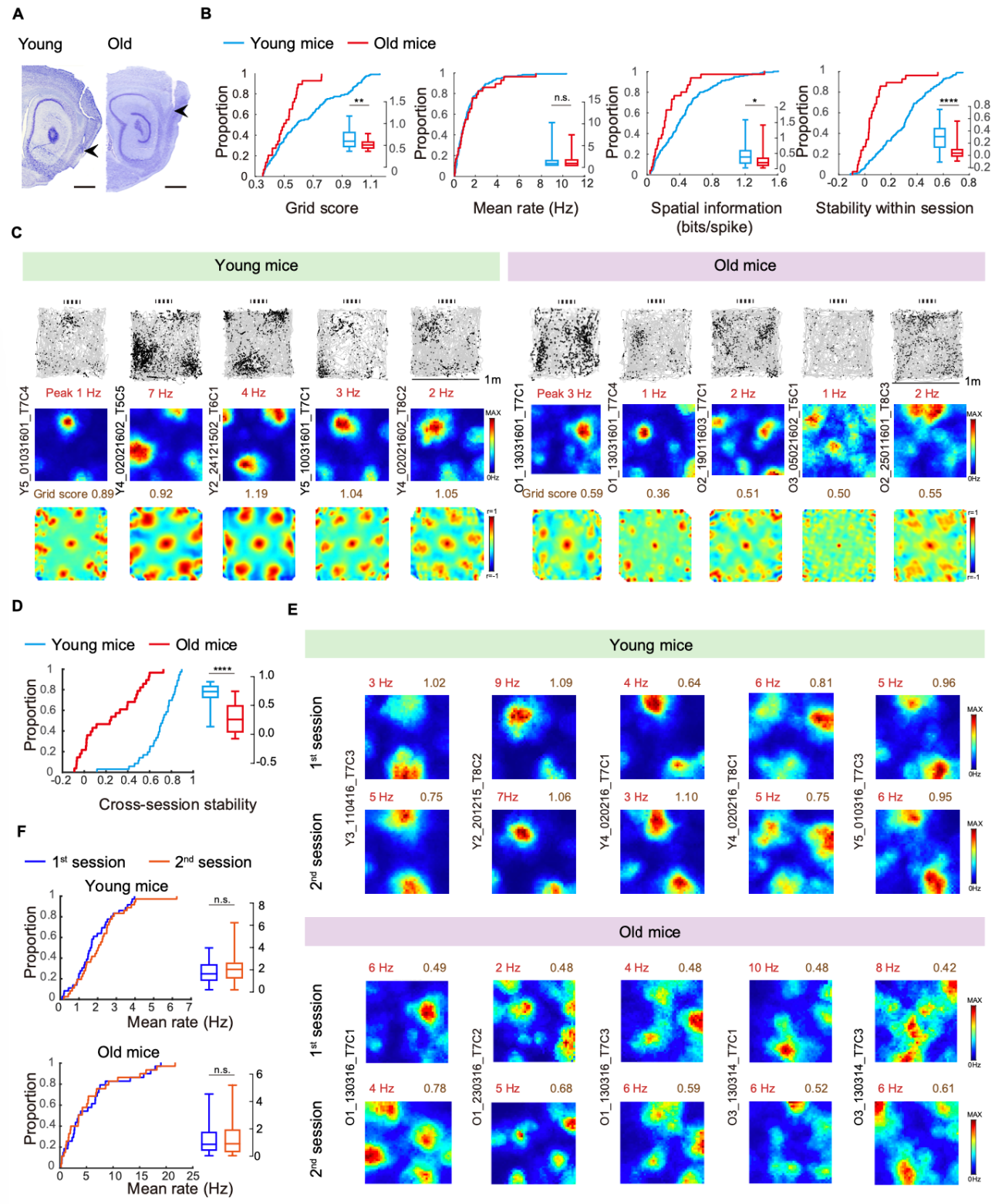

bioRxiv preprint doi: https://doi.org/10.1101/2024.06.27.600930; this version posted July 2, 2024. The copyright holder for this preprint (which was not certified by peer review) is the author/funder, who has granted bioRxiv a license to display the preprint in perpetuity. It is made available under aCC-BY-NC-ND 4.0 International license.

Figure 1. Impaired grid coding and instability across sessions in old mice. (A) Histology showing the tetrode traces in the medial entorhinal cortex (MEC) (sagittal sections). Left, 3 to 4-month-old mouse (young); right, 28-month-old mouse (old); the tetrode locations are indicated by arrows. Scale bar: 1 mm. (B) Cumulative frequency diagrams and box-whisker plots showing a significant decrease in grid score, spatial information, and spatial stability in old mice compared with young mice. (young mice: n = 135, old mice: n = 29; Two sample t-test in grid score: $P = 1.5 \times 10^{-3}$, mean rate: P = 0.69, spatial information: P = 0.012, stability within session: $P = 6.7\times 10^{-8}$). (C) Trajectory map (up), color-coded rate maps (middle), and autocorrelogram (bottom) from grid cells in young (left) and old mice (right). Peak rates (red) and grid scores (brown) are indicated above each rate map and autocorrelogram. Animal and cell numbers are indicated to the left of each triad of rate maps. (D) Cumulative frequency diagrams and box-whisker plots showing a significant decrease in spatial stability across sessions in old mice compared with young mice (young mice n = 36, old mice n = 28; Two sample t-test, $P = 3.8\times 10^{-12}$). (E) Color-coded rate maps of grid cells in the 1st session and 2nd session; peak rates and grid scores are indicated above each rate map. (F) Mean firing rate of grid cells across sessions for young (up) and old (bottom) mice (Kruskal-Wallis test, young mice: P = 0.46; old mice: P = 0.46). Data are presented as mean ± SEM; *** P < 0.001; * P < 0.05; n.s., non-significant. See also Figure S1.

bioRxiv preprint doi: https://doi.org/10.1101/2024.06.27.600930; this version posted July 2, 2024. The copyright holder for this preprint (which was not certified by peer review) is the author/funder, who has granted bioRxiv a license to display the preprint in perpetuity. It is made available under aCC-BY-NC-ND 4.0 International license.

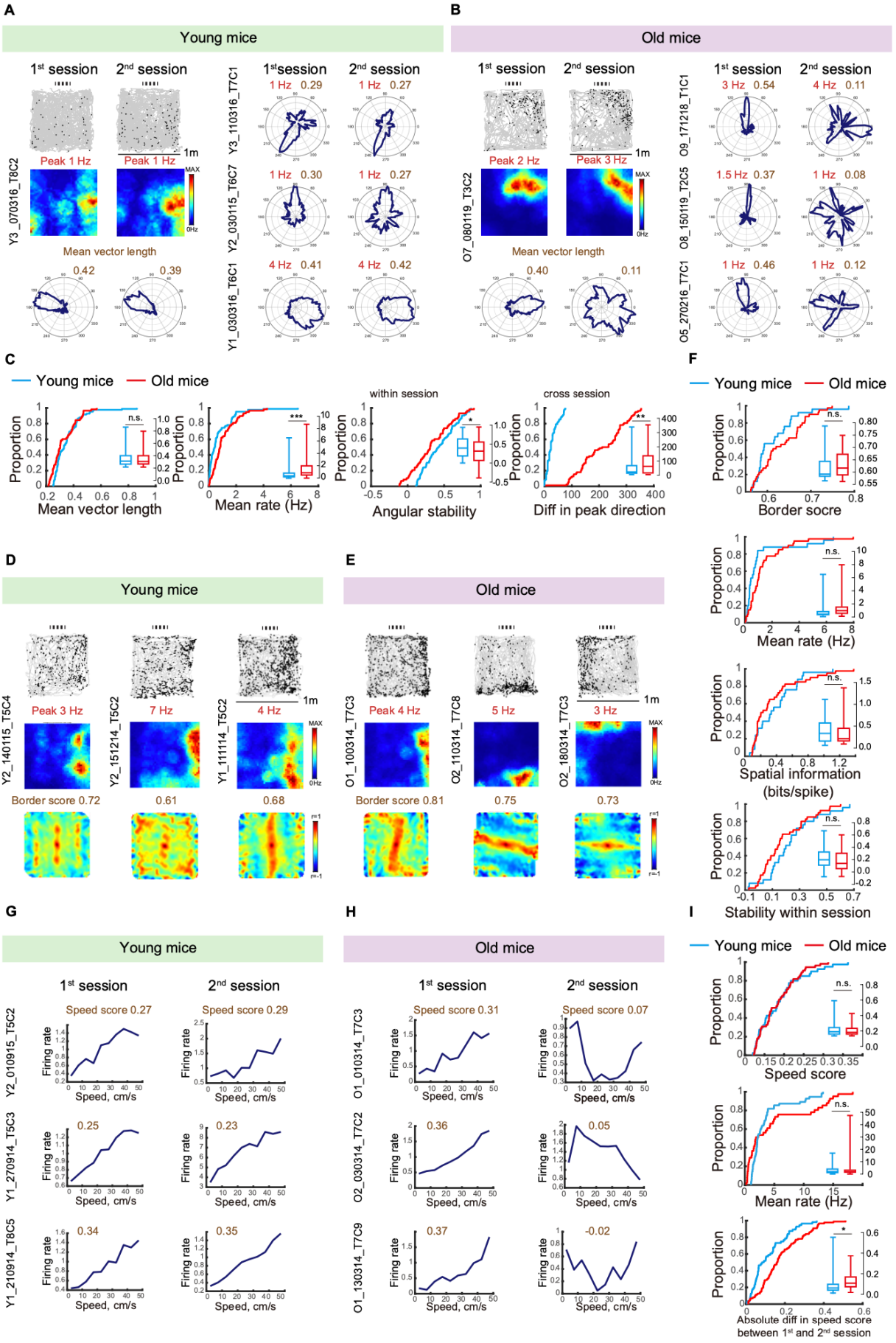

bioRxiv preprint doi: https://doi.org/10.1101/2024.06.27.600930; this version posted July 2, 2024. The copyright holder for this preprint (which was not certified by peer review) is the author/funder, who has granted bioRxiv a license to display the preprint in perpetuity. It is made available under aCC-BY-NC-ND 4.0 International license.

Figure 2. Reduced stability in other spatial cells in old mice. (A) Left: Trajectory map (up), color-coded rate maps (middle), and polar plots indicating firing rate as a function of head direction (bottom) in young mice. Peak firing rate is shown at the top of the rate map and mean vector length is indicated above the polar plot. Animal and cell numbers are indicated to the left of each triad of rate maps. Right: Polar plots of three head direction cells recorded from young mice during two sessions. Peak firing rate and mean vector length are shown at the bottom right of the plot. (B) Head direction cells (HD) in old mice are shown the same way as in (A). (C) Cumulative frequency diagrams and box-whisker plots showing mean vector length and mean rate, within-session angular stability and cross-session peak direction of HD cells in two groups (young mice n = 95, old mice n = 85; Two-sample t-test in Mean vector length: P = 0.94, Mean rate: P = 2.16×10^{-4}, Angular stability: P = 0.024, and Difference in peak direction across sessions: P = 6.63×10^{-3}). (D) Trajectory map (up), color-coded rate maps (middle), and autocorrelogram (bottom) from three border cells in young mice. Peak rates and border scores are indicated above each rate map and autocorrelogram. (E) Three border cells recorded from old mice are shown in the same way as in (D). (F) Cumulative frequency diagrams and box-whisker plots showing border score, mean rate, spatial information and within-session spatial stability in two groups (young mice n = 25, old mice n = 40; Two-sample t-test in Border score: P = 0.19, Mean rate: P = 0.47, Spatial information: P = 0.38, and spatial stability: P =0.26). (G) Speed cells in young mice recorded during two sessions are shown in speed-rate relationship plots; speed scores are shown on top of each plot. (H) Speed cells from old mice recorded during two sessions are shown in the same way as in (G). (I) Cumulative frequency diagrams and box-whisker plots showing speed score, mean rate and absolute difference between speed scores across sessions in two groups (young mice n = 100, old mice n = 37; Two-sample t-test in Speed score: P = 0.54, Mean rate: P = 0.36, and Spatial information: P = 0.03). Data are presented as mean ± SEM; *** P < 0.001; * P < 0.05; n.s., non-significant. See also Figure S2 and S3.

bioRxiv preprint doi: https://doi.org/10.1101/2024.06.27.600930; this version posted July 2, 2024. The copyright holder for this preprint (which was not certified by peer review) is the author/funder, who has granted bioRxiv a license to display the preprint in perpetuity. It is made available under aCC-BY-NC-ND 4.0 International license.

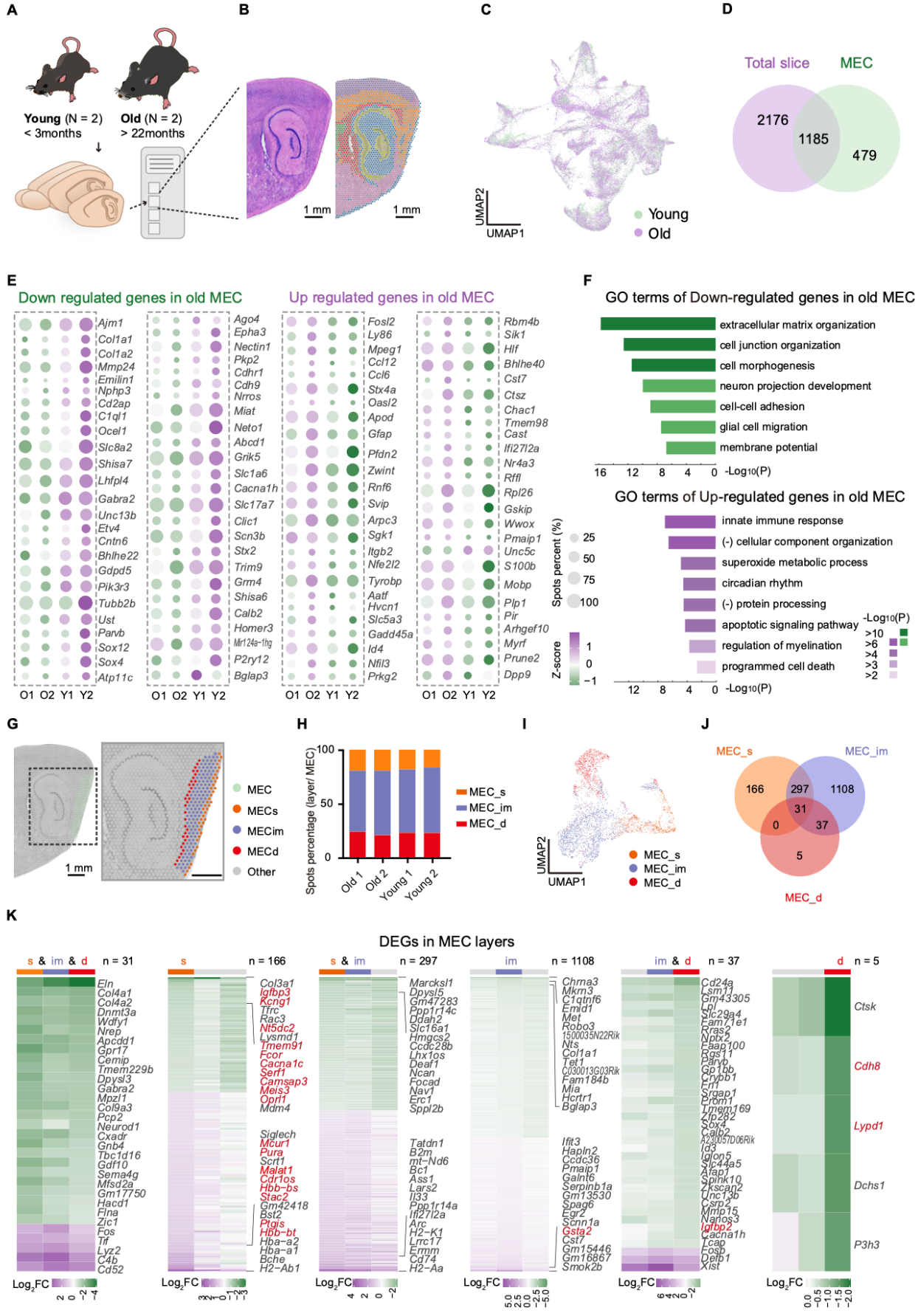

bioRxiv preprint doi: https://doi.org/10.1101/2024.06.27.600930; this version posted July 2, 2024. The copyright holder for this preprint (which was not certified by peer review) is the author/funder, who has granted bioRxiv a license to display the preprint in perpetuity. It is made available under aCC-BY-NC-ND 4.0 International license.

Figure 3. Changes in MEC gene expression profiles during aging using 10x Genomics Visium technology. (A) Streamline schematic of the 10x Genomics Visium experiment. (B) Sagittal sections of young mice brain overlaid with spatial clusters; Scale bar: 1 mm. (C) Uniform manifold approximation and projection (UMAP) map of the factor activities colored by mice from different ages. (D) Venn diagram illustrating the overlap of DEGs between young and old mice across the entire slice and the MEC. (E) 50 selected down or up-regulated genes in old MEC are displayed in dot plot. Dot size shows percentages of spots where that specific gene is expressed in whole MEC spots. Expression levels of genes are indicated by Z-score. (F) Bar graph showing the enrichment GO terms of down and up-regulated genes in old MEC, using a discrete color scale to represent statistical significance ($-Log_{10}(P)$). (G) Example of manually defining MEC and its sublayers based on H&E staining brain slice: MEC_s, MEC_im and MEC_d. (H) Percentage bar plot showing distributions of spots from three sublayers of MEC among all the MEC spots in four mice samples. (I) UMAP of MEC spatial spots colored by their assigned regions. (J) Venn diagram showing the number of DEGs of old and young mice discovered in three sublayers of MEC. (K) DEGs are found from only one, two or both layers in MEC. The first, fifth and sixth columns show the whole genes and the rest show the top 15 genes from both up and down-regulated DEGs. Genes that were not discovered in the entire MEC DEGs lists are highlighted in red. Expression level shows higher expression in old mice with higher absolute scores of Log_2 Fold Change. See also Figure S5 – S8 and Table S1 - S3.

bioRxiv preprint doi: https://doi.org/10.1101/2024.06.27.600930; this version posted July 2, 2024. The copyright holder for this preprint (which was not certified by peer review) is the author/funder, who has granted bioRxiv a license to display the preprint in perpetuity. It is made available under aCC-BY-NC-ND 4.0 International license.

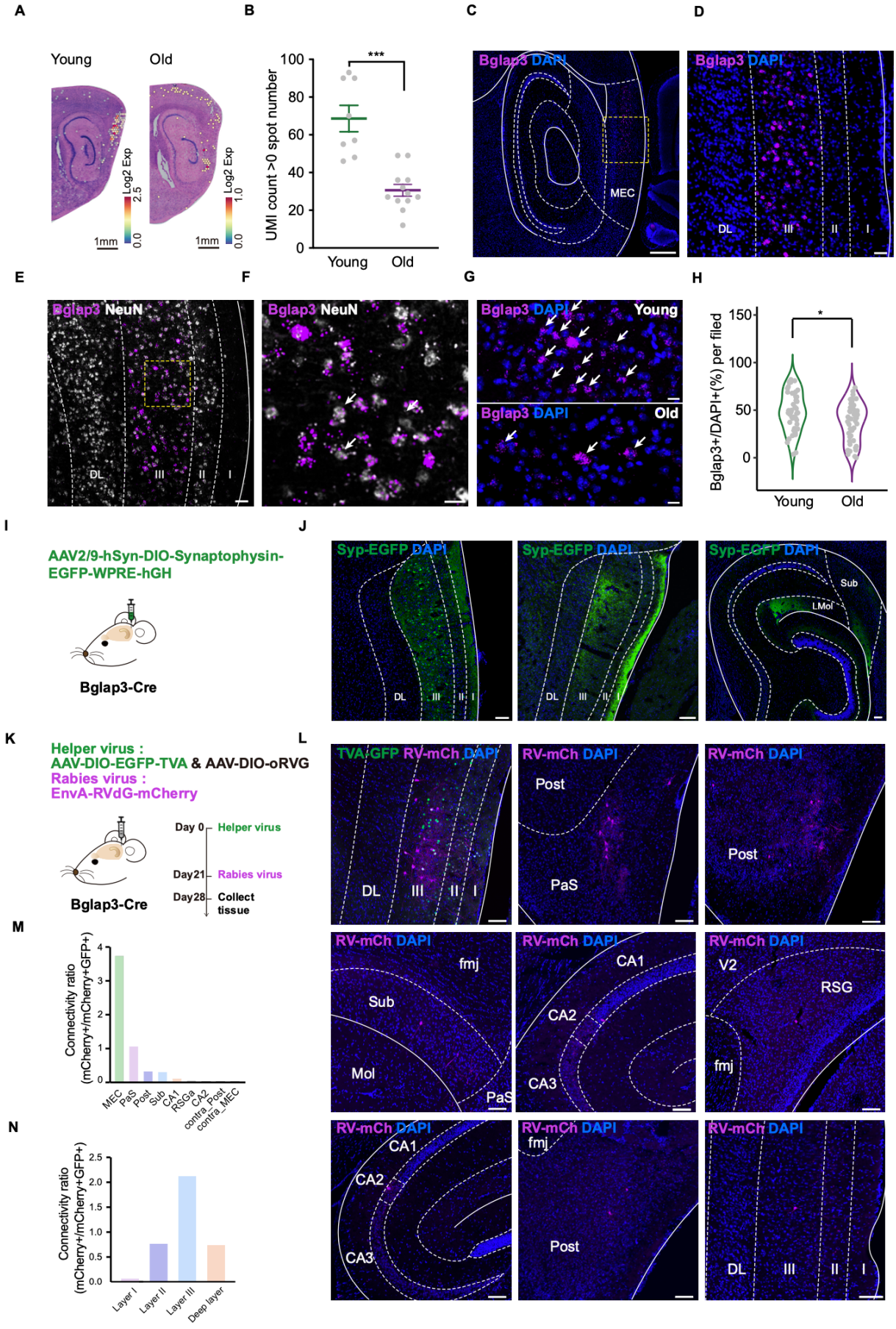

bioRxiv preprint doi: https://doi.org/10.1101/2024.06.27.600930; this version posted July 2, 2024. The copyright holder for this preprint (which was not certified by peer review) is the author/funder, who has granted bioRxiv a license to display the preprint in perpetuity. It is made available under aCC-BY-NC-ND 4.0 International license.

Figure 4. The number of Bglap3+ cells is decreased in old mice. (A) 10x Genomics Visium data shows the specific expression of Bglap3 in MEC. (B) UMI count shows the decreased number of Bglap3+ spots in the MEC during aging (n = 8 regions from 2 young mice, n = 12 regions from 2 old mice, two-tailed Mann–Whitney U-test, P = 0.0002). (C) *In situ* hybridization (ISH) displays a specific expression of Bglap3 in Layer III of the MEC; the amplified view of the yellow window in (C) is shown in (D); the pink signal represents Bglap3 and the blue signal represents DAPI. (E) Bglap3 is specifically expressed in NeuN+ neurons in Layer III of the MEC; the amplified view of the yellow window in (E) is shown in (F); the pink signal represents Bglap3 and the white signal represents NeuN. (G) Decreased number of Bglap3+ cells in the MEC of old mice; white arrows show the Bglap3+ cells. (H) Count of the Bglap3+ cells in the ISH data shows a significantly decreased number of Bglap3+ cells in the MEC of old mice (n = 45 fields from 4 young mice and n = 45 fields from 4 old mice, young mice vs. old mice, two-tailed Mann–Whitney U-test, P = 0.0232). (I) The axons of Bglap3+ cells are labeled by synaptophysin-EGFP. (J) The axons mainly existed in the ipsilateral MEC (middle panel) and the prefrontal pathway in the hippocampus (right panel); the green signal is the soma and axon of the infected Bglap3+ cells and the blue signal is DAPI. (K) The experimental diagram shows the rabies virus infection of Bglap3+ cells to label their presynaptic cells with mCherry. (L) Representative image shows the presynaptic cells to the Bglap3+ cells in different brain areas, including the MEC, parasubiculum (PaS), postsubiculum (Post), subiculum (Sub), hippocampus CA1, CA2, retrosplenial cortex (RSG), contralateral postsubiculum (contra_Post) and contralateral MEC (contra_MEC). (M) Histogram shows the distribution of the presynaptic cells to the Bglap3+ cells in different brain areas. (N) Histogram shows the distribution of the presynaptic cells to the Bglap3+ cells in different layers of the MEC. Data are presented as mean ± SEM; *** P < 0.001; * P < 0.05; n.s., non-significant. Scale bars shown in (A): 1 mm, (C): 500 μm, (D): 50 μm, (E): 50 μm, (F): 20 μm, (G): 20 μm, (J): 100μm; (L): 100 μm. See also Figure S9.

bioRxiv preprint doi: https://doi.org/10.1101/2024.06.27.600930; this version posted July 2, 2024. The copyright holder for this preprint (which was not certified by peer review) is the author/funder, who has granted bioRxiv a license to display the preprint in perpetuity. It is made available under aCC-BY-NC-ND 4.0 International license.

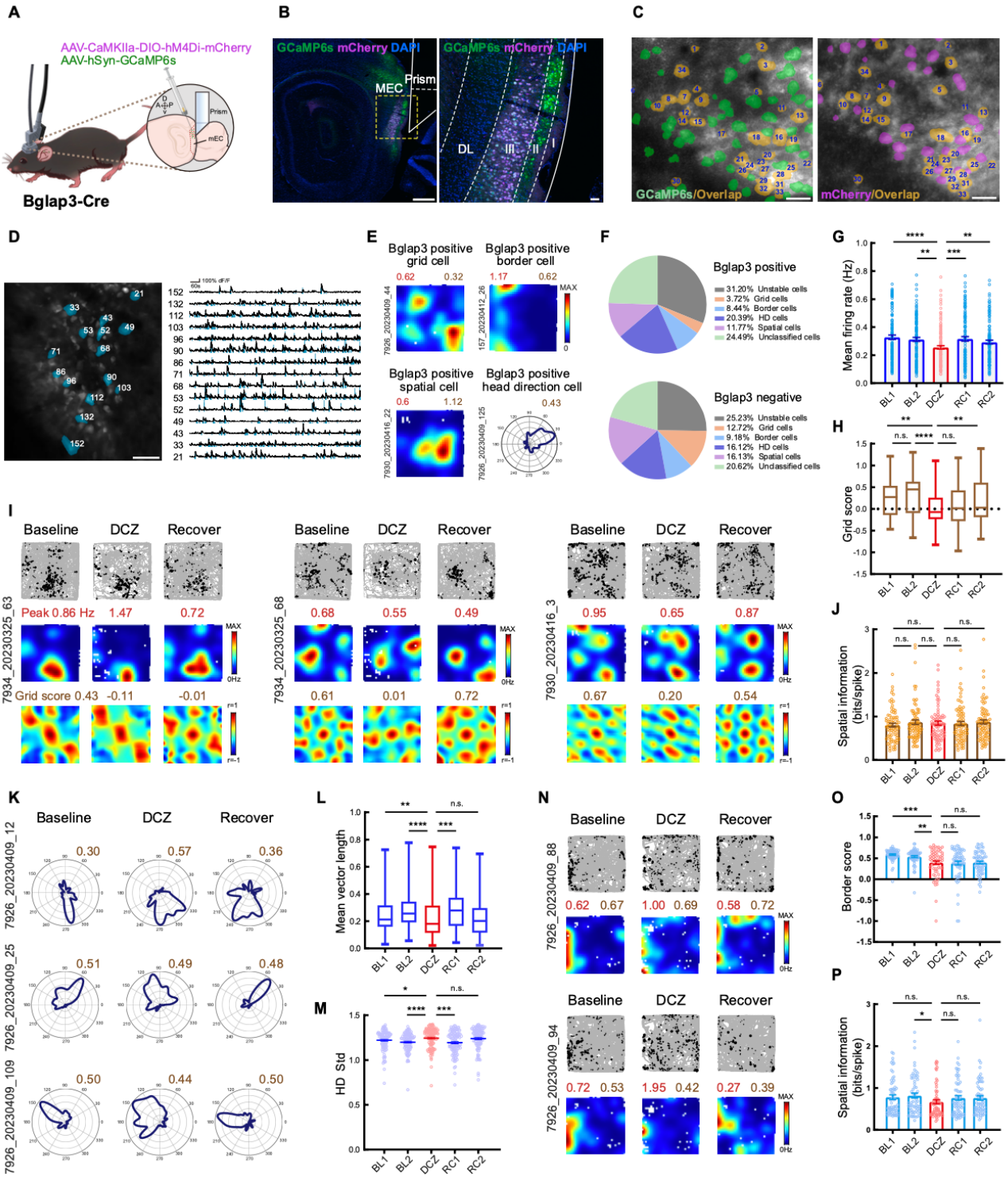

bioRxiv preprint doi: https://doi.org/10.1101/2024.06.27.600930; this version posted July 2, 2024. The copyright holder for this preprint (which was not certified by peer review) is the author/funder, who has granted bioRxiv a license to display the preprint in perpetuity. It is made available under aCC-BY-NC-ND 4.0 International license.

Figure 5. Inactivation of Bglap3+ cells impaired the grid and spatial coding in MEC. (A) Cartoon of the 2-photon imaging of Bglap3+ cells in the MEC showing a miniaturized 2-photon microscope (TPM) in freely behaving mice and the prism location in the brain. (B) The expression of GCaMP6s (green) in superficial MEC and DIO-hM4D-mCherry (magenta) in Bglap3+ cells of imaging mouse; the white outline indicates the position of the prism. The amplified view of the yellow window in the left panel is shown in the right panel. LI: Layer 1; LII: Layer 2; LIII: Layer 3; DL: Deep layer. (C) Example images represent the field of view (FOV) of the miniaturized TPM, with >200 cells (color-coded dots) identified in a freely behaving mouse. GCaMP6s+ cells are shown in green (left panel); Bglap3+ cells are labeled with mCherry (right panel); the co-labeled cells are shown in orange and marked with numbers. (D) FOV of Ca^{2+} imaging (left panel) and the raw traces of fluorescence changes (ΔF/F) for the 15 cells outlined in the left panel (right panel). (E) Representative rate map showing example grid cells, border cells, head direction cells, and unclassified spatial cells from Bglap3+ cells. (F) Pie chart showing the proportion of different functional cell types in Bglap3 positive and negative populations. (G) DCZ injection induced a significantly decreased mean firing rate of Bglap3+ cells. (H) Histogram showing decreased grid scores after inhibition of Bglap3+ cells (n = 77 cells from 6 mice). (I) Grid cells before, during, and after DCZ injection, with trajectory maps (top), representative color-coded rate maps (middle), and autocorrelograms (bottom) from grid cells; peak rates (red) and grid scores (brown) are indicated above each rate map; animal and cell numbers are indicated to the left of each triad of rate maps. (J) Spatial information of grid cells does not exhibit clear changes after DCZ injection. (K) Polar plots of head direction cells before, during, and after DCZ injection, indicating firing rate as a function of head direction (blue); mean vector length (brown) is indicated above the polar plot; animal and cell numbers are indicated to the left of each triad of rate maps. Mean vector length (L) and circular standard deviation in radians (M) from head direction cell data before, during, and after DCZ injection (n = 110 cells from 6 mice). (N) Border cells before, during, and after DCZ injection, with trajectory maps (top) and representative color-coded rate maps (bottom) from border cells. (O) Border scores of border cells before, during, and after DCZ injection (n = 65 cells from 6 mice). (P) Spatial information of border cells before, during, and after DCZ injection. Data are presented as mean ± SEM;

bioRxiv preprint doi: https://doi.org/10.1101/2024.06.27.600930; this version posted July 2, 2024. The copyright holder for this preprint (which was not certified by peer review) is the author/funder, who has granted bioRxiv a license to display the preprint in perpetuity. It is made available under aCC-BY-NC-ND 4.0 International license.

*** P < 0.001; ** P < 0.01; * P < 0.05; n.s., non-significant. Scale bars in B, C and D are 500, 50 μm, 20, 20μm, 20 μm, respectively. See also Figure S10 - S13.

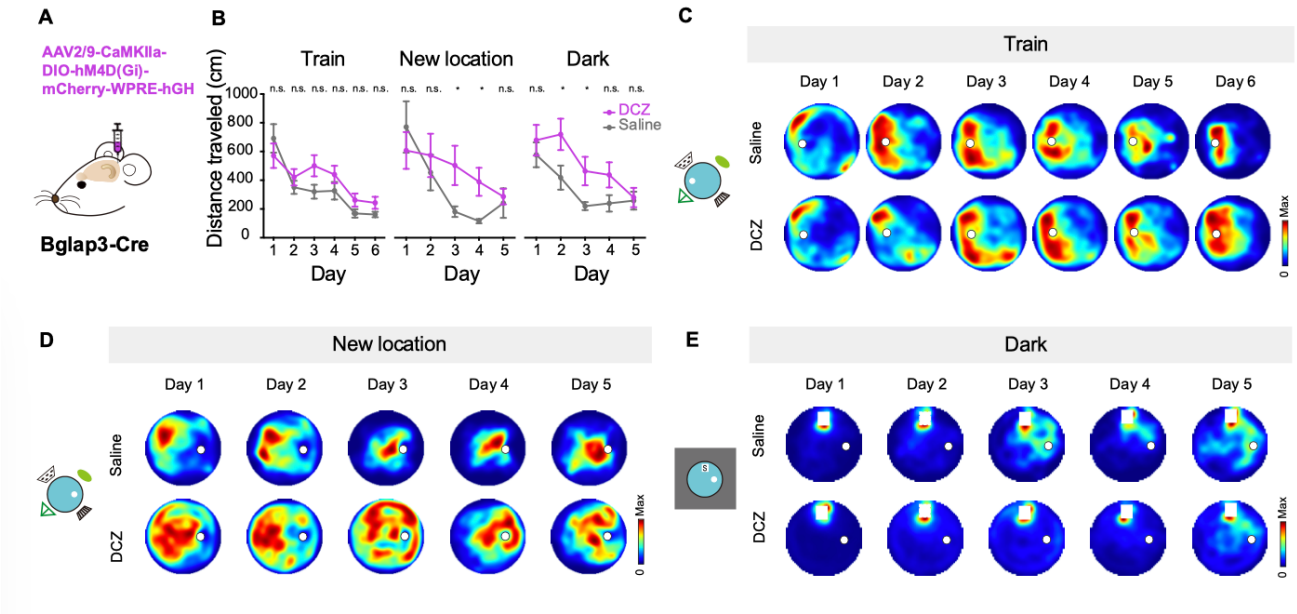

Figure 6. Chemogenetically silencing of Bglap3+ cells impaired the spatial performance in young mice. (A) The cartoon depicts hM4D infection in the mouse MEC to label Bglap3+ cells. (B) Water maze learning curves of mice in the training (Train, left panel), cue relocation in light (New location, middle panel), and dark sessions (Dark, right panel) after inactivation of Bglap3+ cells with DCZ, which resulted in impaired learning in the cue relocation experiment under light and dark conditions (n = 20 trials from DCZ group, n = 16 trials from Saline group). (C) Color-coded heatmap shows the performance in the water maze during 6 days of training between saline (top) and DCZ (bottom) groups. Maximum exploration time is indicated in red. (D, E) Color-coded heatmap as in (C) showing behavior performance in the platform relocation experiment in light and dark conditions. Data are presented as mean ± SEM; *** P < 0.001; ** P < 0.01; * P < 0.05; n.s., non-significant. See also Figure S14.